Robust Emergency Fast Discharge Algorithm for Lithium-Ion Batteries

Iman Ebrahimi[a], Vivian Tran[b], Anna Stefanopoulou[b], Ricardo de Castro[a]

[a]*Department of Mechanical Engineering, University of California, Merced, 5200 North Lake Rd, Merced, CA 95343, California, USA*
[b]*Department of Mechanical Engineering, University of Michigan, 2350 Hayward, Ann Arbor, MI 48109, Michigan, USA*

Abstract

This paper proposes a new control algorithm to manage emergency discharge of batteries, quickly reducing their state of charge and the likelihood of thermal runaway. This emergency discharge can lead to a hazardous process, especially if the discharge rate induces high ohmic heat generation that in turn increases the degeneration rate of the solid electrolyte interphase (SEI), which may lead to venting and rupture of the pouch cell. To mitigate these risks, we propose a Control Barrier Function (CBF)-based algorithm to enforce safety during this emergency discharge; and a state estimator based on Extended Kalman Filter (EKF) to predict unmeasurable states, such as molar fraction of SEI layer decomposition, which is a critical information to guarantee safety during quick discharges. The effectiveness of the controller is validated with a Single-Particle Model with electrolyte (SPMe) model and its robustness analyzed via Monte Carlo methods.

Keywords: Battery Emergency Discharge, Battery Safety, Control Barrier Functions, State Estimation, SPMe, Monte Carlo Simulations

---

1. Introduction

Recent incidents underscore the critical safety challenges associated with lithium-ion batteries. In January 2025, a large fire at the Vistra Energy lithium battery plant in Moss Landing, California, forced the evacuation of up to 1,500 residents due to toxic smoke. The fire, difficult to extinguish due to the chemistry of lithium-ion cells, was allowed to burn out naturally [1]. In 2020, an explosion at an Arizona Public Service (APS) facility in Surprise, Arizona, was traced to thermal runaway, which generated flammable gases that later ignited [2, 3]. Similarly, in 2021, an electric bus depot fire in China spread rapidly to nearby vehicles after battery venting released flammable gases, demonstrating the potential for fire propagation in dense parking spaces [4].

These events highlight two coupled hazards in lithium-ion batteries: *thermal runaway* and *venting*. Thermal runaway occurs when heat generation exceeds dissipation, producing a self-accelerating temperature rise that can cause fire [5]. Venting releases flammable or toxic gases, often triggered by overpressure from electrolyte decomposition or other internal reactions, and can escalate fire spread in battery packs [6]. Both phenomena may be initiated by electrical, mechanical, or thermal abuse [7], including overcharging, physical damage, manufacturing defects, prolonged exposure to high temperatures, or high-current discharge from internal or external shorts [8].

Emergency discharge is a possible countermeasure in such scenarios. As discussed in [9, 10], lowering the battery's State-of-Charge (SoC) reduces stored energy and limits the severity of thermal events. When fast discharge is applied to cells that remain structurally intact (but are at risk of experiencing abuse), it can help prevent the propagation of fire and thermal runaway events by removing energy from modules at high risk. Empirical studies show that low-SoC cells release far less energy during abuse, reducing flame intensity and propagation [10, 11]. Reflecting these findings, U.S. Department of Transportation regulations limit the SoC of lithium-ion batteries to 30% for air transport [12].

Executing rapid discharge of batteries introduces its own safety challenges. High currents generate heat, accelerates degradation, and electrolyte decomposition can lead to venting [13]. To promote battery safety, standard battery management systems (BMSs) usually enforce electro-thermal constraints, including manufacturer-prescribed voltage/current limits, SoC limits to prevent under- and over-discharge, and maximum temperature for thermal safety [14]. However, these standard BMSs aim to operate the battery well below the *venting limits*. For rapid emergency discharge, batteries need to operate at (or close) to the *venting limits*. The design of battery control algorithms to operate at these *venting limits* has received limited attention in the literature; this is an area within battery controls that is still in its infancy.

1.1. The Battery Control Contribution

The first control algorithms for fast battery discharge at *venting limits* relied on Model Predictive Control (MPC) methods [15, 16]. This approach is able to enforce multiple safety constraints, while optimizing performance metrics (e.g., discharge time). It offers an effective methodology for this control problem, but requires high computation effort, which complicates its deployment onboard embedded systems with limited computational power.

Control Barrier Functions (CBFs) are another attractive methodology [17]. They rely on set invariance methods to keep system states within pre-defined safe limits, and usually require low computational effort, making them particularly attractive for real-time embedded systems. In the battery domain, CBFs have been recently applied to fast charging [18, 19], where they optimize safety and charging time under electro-thermal constraints focusing on normal battery operation. However, these previous works did not address venting or gas generation constraints that become critical in emergency discharge scenarios. Our work addresses this shortcoming by providing a new CBF-based formulation that enforces not only electro-thermal constraints, but also *venting limits*. To the best of our knowledge, this is the first time that *venting limits* are proposed within a CBF-based control framework for batteries. Additionally, we demonstrate that the CBF-based formulation is able to provide the same level of discharge performance and constraint satisfaction as state-of-the art MPC approaches, while decreasing the overall computational time by more than 15x.

1.2. The Battery Estimation Contribution

To quickly discharge of batteries at *venting limits*, control algorithms need access to key battery states that are not directly measured, e.g., SoC, internal cell temperature and Solid-Electrolyte Interphase (SEI) decomposition. To address this need, several estimation approaches have been proposed in the literature to predict SoC [20, 21] and internal cell temperature [22, 23]. However, estimating SEI decomposition - a crucial factor contributing to battery venting - has received less attention.

SEI is a layer that is formed on the anode of Li-ion cells during the initial charging cycles [24]. It is one of the most thermally sensitive elements in Li-ion cells, and can begin to decompose when the internal temperature reaches 80 °C [25]. This decomposition leads to the release of gases (e.g., carbon dioxide and hydrogen) [26], vaporization of the electrolyte and increases internal pressure. Once the internal pressure exceeds a “critical threshold”, the cell’s valve opens, releasing gases (venting) that are often highly flammable [27]. Since this venting process is mainly driven by the SEI decomposition, it is crucial to monitor and estimate this state during the emergency discharge.

Previous research has directly measured SEI decomposition using invasion techniques, involving *post-mortem* disassembly in an inert environment and analysis with expensive laboratory equipment such as X-ray photoelectron spectroscopy (XPS) or scanning electron microscopy (SEM) [28]. However, these techniques are not suitable for the real-time monitoring of batteries deployed in real-world applications, such as onboard an electric vehicle. Another approach, which is less invasive, involves using Electrochemical Impedance Spectroscopy (EIS) [29, 30]. Within this framework, the SEI layer is modeled using an equivalent resistance and capacitance that affect the high-frequency response of the battery. This method requires injecting a (small) sinusoidal current into the battery across a range of frequencies; the resulting voltage response is measured, and parametric optimization methods [31] are then used to fit the measured frequency response. The downside of this approach is the requirement for a probing current, necessitating dedicated electronics integrated and deployed within the battery system—a practice that is not yet widely adopted in industry.

To address these shortcomings, our paper proposes a virtual sensing approach, based on Extended Kalman Filter (EKF) [32], to estimate SEI decomposition. This new approach only requires non-invasive measurements of temperature, voltage and battery expansion, along with a reduced-order model of the SEI decomposition and internal battery pressure. Unlike EIS-based methods, our virtual sensing approach does not require additional electronics for generating probing currents. To the best of the authors’ knowledge, it is the first time that such virtual sensing formulation is proposed in the literature.

1.3. Summary of Contributions

We propose a novel CBF-based framework to quickly discharge batteries at *venting limits*.

- To enable the implementation of venting constraints in the CBF framework, we propose a polynomial approximation of the battery pressure model, which allows us to reduce modeling complexity. Based on this formulation, we derive sufficient conditions associated with *venting limits* that guarantee the numerical feasibility of the CBF’s safe control set. Additionally, we apply robust methods to the CBF framework to enforce safety constraints in the presence of model uncertainty.

- We propose a new EKF-based method to estimate SEI decomposition during fast discharge. We perform an observability analysis to determine the feasibility of using non-invasive measurements (voltage, temperature, and battery expansion) and a reduced-order mechanical/gas model to estimate this critical state that drives battery venting.

- The robustness of the emergency discharge controller is evaluated through extensive Monte Carlo simulations. A sensitivity analysis is conducted by evaluating the impact of multiple parameter uncertainty in the enforcement of venting safety constraints. The final design is validated through simulations on a physics-based Single Particle Model with Electrolyte (SPMe) model, developed in PyBaMM.

This work extends our previous study [16] by including additional theoretical analysis to ensure numerical feasibility of the CBF controller and robust extensions that account for model uncertainties. A significant addition is the development of an EKF to estimate internal battery states (such as SEI decomposition), which were previously assumed to be known. These enhancements are verified through extensive simulations using a high-fidelity SPMe model, whereas the conference paper [16] relied on a low-fidelity model for both design and validation.

2. Overview of the Emergency Battery Discharge

Figure 1 provides an overview of the battery’s discharge process. Our (ego) battery is assumed to be located in close proximity to another battery that may undergo a thermal runaway

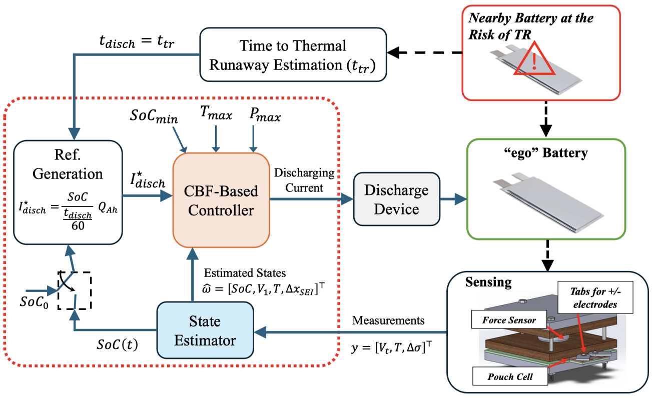

Figure 1: Overview of the emergency discharge process. We assume that our (ego) battery is in close proximity to another battery at the risk of thermal runaway (TR). We focus on the design of the control and estimation algorithms (dashed red box) to quickly and safely discharge the ego battery.

(TR) event, potentially subjecting the ego battery to thermal, mechanical, or electrical abuse. We assume the existence of an algorithm capable of predicting the time to thermal runaway (t_{TR}), such as those described in [33, 34]. If such an estimator is not available, industrial guidelines may be considered. For example, a recent NHTSA study [35] suggests that commercial light-duty electric vehicles need between 22 and 177 minutes to develop external flames in response to battery abuse.

Our objective is to discharge the ego battery within a duration $t_{disch} \leq t_{TR}$. This ensures that when the expected abuse occurs (e.g., due to the TR of the neighboring battery), the SoC is low and the 'ego' battery presents fewer safety risks. To implement this emergency discharge, four main elements must be implemented. First, a reference discharge current ($I^{\star}_{\mathrm{disch}}$) is determined to reduce the SoC of the ego battery within the available time t_{disch}. This can be computed as:

$$I^{\star}_{disch} = \frac{SoC}{t_{\mathrm{disch}}/60} Q_{Ah}, \tag{1}$$

where Q_{Ah} is the cell capacity in Ah and t_{disch} is the target discharge time in minutes. Note that this reference current can be computed at the beginning of the discharge process, and then kept constant until the discharge is completed. Alternatively, it can also be continuously adapted based on the current SoC and t_{TR}.

Second, this reference current $I^{\star}_{disch}$ is adjusted through a CBF framework, ensuring that the discharge current is safe and fulfills electrical, thermal, and venting constraints. Third, a virtual EKF-based estimator is utilized to provide real-time estimates of internal states that are not directly measurable (such as SEI decomposition). Fourth, a discharge device de-energizes the ego battery by implementing the safe discharge current.

One important practical consideration deals with the realization of the discharge device. For small-scale batteries, the device may consist of a dissipative resistor connected to an electronic switch, allowing for the regulation of the average discharge current via switching control. For larger battery systems, a power converter is likely required to manage the energy, for example, by injecting the discharge energy into the power grid [36]. In the following sections, we assume such a discharge device is available and focus on the design of the controller and estimator components (highlighted by the dashed red box in Figure 1).

The next two sections describe the modeling framework and the proposed controller for the fast-discharge method.

3. Modeling

This section introduces the battery modeling approach. Two models are considered: first, a low-fidelity Equivalent Circuit Model (EqCM), which features reduced complexity and is used for control design; and second, a physics-based SPMe, utilized for validation purposes.

3.1. Equivalent Circuit Model (EqCM)

As depicted in Figure 2, the battery model can be divided into three sub-systems, including i) the electrical model, which captures the voltage and SoC response of the battery using an EqCM; ii) the thermal model; and iii) the gas pressure model.

3.1.1. Electric Model

To model the electrical dynamics, the EqCM uses an equivalent circuit composed of a series resistor R_s, an open-circuit voltage source $V_{OCV}(SoC)$, and one series RC pair, as shown in Figure 3, with a voltage drop V_1. The dynamics of SoC and V_1 are described as:

$$S\dot{o}C(t) = -\frac{\eta(t)}{Q} I(t), \tag{2a}$$

$$\dot{V}_1(t) = -\frac{V_1(t)}{R_1 C_1} + \frac{I(t)}{C_1}, \tag{2b}$$

where Q is the cell capacity, $I(t) \geq 0$ is the discharging current, and $\eta(t)$ is the Coulombic efficiency. In this work, we make the standard assumption that $\eta(t) = 1$ during discharge [37]. The terminal voltage of the battery can be computed via Kirchhoff's voltage law:

$$V_t(t) = V_{OCV}(SoC(t)) - R_s I(t) - V_1(t). \tag{3}$$

3.1.2. Thermal Model

To model the battery temperature (T), we assume a lumped thermal capacitance (C_p) and convective heat transfer between the battery and the environment (T_{amb}):

$$m_{cell} C_p \dot{T}(t) = \left(\dot{Q}_{\mathrm{ohmic}} + \dot{Q}_{\mathrm{SEI}}\right) - h A_{\mathrm{surf}}(T(t) - T_{amb}), \tag{4}$$

where m_{cell} is the cell mass, h is the effective convective heat transfer coefficient, and A_{surf} is the cell cooling area. This thermal model assumes that the heat generated ($\dot{Q}_{gen}$) in the battery is caused by Joule losses ($\dot{Q}_{ohmic}$) and SEI decomposition ($\dot{Q}_{\mathrm{SEI}}$):

$$\dot{Q}_{\mathrm{ohmic}} = I(V_{OCV}(SoC) - V_t) = I^2 R_s + I V_1, \tag{5a}$$

$$\dot{Q}_{\mathrm{SEI}} = -m_{an} h_{\mathrm{SEI}} \dot{x}_{\mathrm{SEI}}, \tag{5b}$$

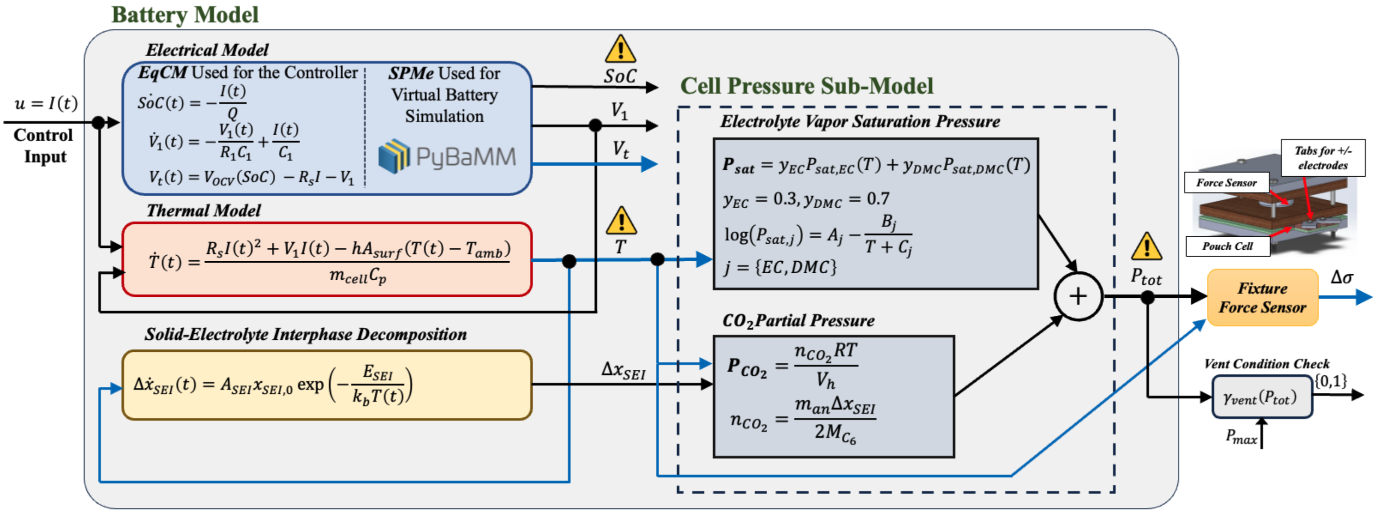

Figure 2: Battery model overview. The model is divided into multiple sub-models, including the electro-thermal domain, theSEI decomposition, and the cell's internal pressure. Hazard icons indicate states subject to safety constraints in our formulation. Signals in blue denote measured variables.

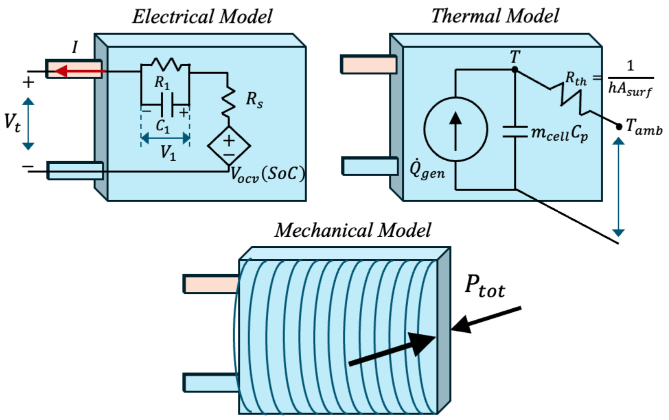

Figure 3: Electro-thermal equivalent circuit diagrams.

where $\dot{x}_{\text{SEI}}$ and h_{SEI} are the rate and enthalpy of the SEI decomposition reaction [38], respectively, and m_{an} is the mass of the anode. For control design purposes, the term $\dot{Q}_{\text{SEI}}$ is neglected since typically $\dot{Q}_{\text{ohmic}} \gg \dot{Q}_{\text{SEI}}$ (see [38] and Fig. 3 in [15]). Other heat generation components, such as the heat absorption term from electrolyte vaporization, are neglected in this study because their contributions are negligible compared to ohmic losses at high currents. [39]

3.1.3. Pressure Model

The total gas pressure of the battery cell is determined by two terms: the saturation pressure of the electrolyte (P_{sat}), and the pressure generated by SEI decomposition and CO_2 gas (P_{CO_2}). Mathematically, this means:

$$P_{tot}(t) = P_{sat}(t) + P_{CO_2}(t). \tag{6}$$

The first term, electrolyte vapor saturation pressure, assumes a 3:7 (% Vol) ethylene carbonate (EC) to dimethyl carbonate (DMC) electrolyte. The partial pressure of each component is computed according to the Antoine equation:

$$P_{sat}(t) = \sum_{j=\{EC,DMC\}} y_j \times 10^{A_j - \frac{B_j}{T(t)+C_j}}, \tag{7}$$

where y_j is the mole fraction of each electrolyte component, and the coefficients A_j, B_j, C_j for $j = \{EC, DMC\}$ are known parameters [40].

To capture SEI-driven gas generation, we assume CO_2 is the dominant first-vent species and model SEI decomposition with a self-limiting Arrhenius rate [15, 39]. The reaction pathway is

$$(CH_2OCO_2Li)_2 \rightarrow Li_2CO_3 + C_2H_4 + CO_2 + \frac{1}{2}O_2. \tag{8}$$

Define x_{SEI} as the mole fraction of Li residing in the SEI relative to the total moles of negative-electrode active material (C_6). The SEI decomposition (Δx_{SEI}) and CO_2 accumulation (n_{CO_2}) are then defined as:

$$\Delta x_{\text{SEI}}(t) = x_{\text{SEI},0} - x_{\text{SEI}}(t), \tag{9a}$$

$$\Delta\dot{x}_{\text{SEI}}(t) = A_{\text{SEI}}x_{\text{SEI},0}\exp\left(-\frac{E_{\text{SEI}}}{k_bT(t)}\right), \tag{9b}$$

$$x_{\text{SEI}}(0) = x_{\text{SEI},0}, \quad 0 \leq x_{\text{SEI}} \leq x_{\text{SEI},0} \tag{9c}$$

$$n_{CO_2}(t) = \frac{m_{an}\Delta x_{\text{SEI}}}{2M_{C_6}}, \tag{9d}$$

where $x_{\text{SEI},0}$ is the initial value of the $x_{\text{SEI}}(t)$ state, A_{SEI} is the frequency factor for SEI decomposition, E_{SEI} is the activation energy, k_b is Boltzmann's constant, m_{an} is the mass of the negative electrode, M_{C_6} is the molar mass of C_6, and the factor $\frac{1}{2}$ follows from the stoichiometry. With the ideal-gas assumption in the headspace volume $V_h(t)$, we obtain the CO_2 pressure:

$$P_{CO_2}(t) = \frac{n_{CO_2}(t)RT(t)}{V_h(t)}, \tag{10}$$

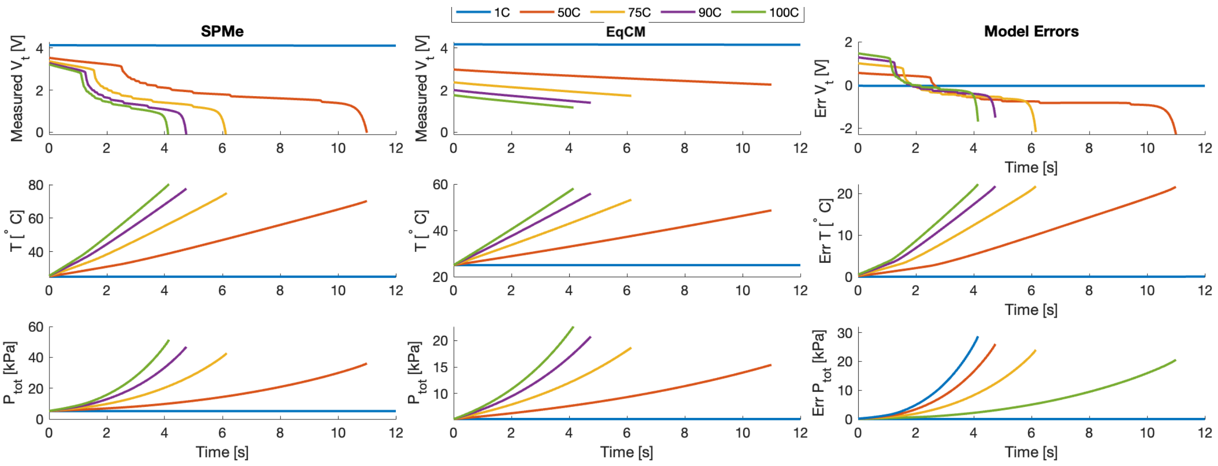

Figure 4: Model Comparison: SPMe vs. equivalent circuit model for a range of discharge c-rates from 1C to 100C. First Column: SPMe, Middle Column: EqCM, Right Column: Fitting error (i.e., difference between SPMe and EqCM states). .

where R is the ideal gas constant. The headspace volume along the edges of the pouch cell can be computed as

$$V_h(t) = V_{h,0} + A_{\text{surf}}\left(\frac{L\Delta\sigma(t)}{E} - \alpha_{cell}\Delta T(t)\right), \tag{11}$$

where ΔT is the change in temperature from the initial cell temperature, i.e., $\Delta T(t) = T(t) - T_{amb}$, E is Young's modulus, L represents the nominal thickness of the compliant poron layers that deform in response to cell swelling, and α_{cell} denotes the effective thermal expansion coefficient . The compressive stress in the battery cell fixture, $\Delta\sigma(t)$, accounts for both gas pressure and thermal swelling of the cell. It is defined as [15] and [40] :

$$\Delta\sigma(t) = \max\left(\underbrace{P_{tot} - \sigma_0 - P_{atm}}_{\text{gas pressure}}, \underbrace{\frac{E\alpha_{cell}\Delta T}{L}}_{\text{solid pressure}}\right) \tag{12}$$

where σ_0 is the initial compressive stress applied by the fixture, and P_{atm} the atmospheric pressure.

3.2. Single Particle Model with Electrolyte (SPMe)

The SPMe is a physics-based model that represents each battery electrode as a single spherical porous particle, while including electrolyte dynamics [41]. SPMe is more accurate than the EqCM as it is being capable of capturing the transition from normal to diffusion-limited discharge - a phenomenon especially relevant for high-current discharge [39]. However, the SPMe requires significantly higher modeling and parameterization complexity than the EqCM. In this work we employ the SPMe, derived in [41] and extend it with a venting model from [39, 42], for validation purposes.

Figure 4 compares the states and outputs of the EqCM and SPMe, fitted with experimental data from an external short circuit (see Appendix A for details). In these results, the simulations were terminated when the SPMe model terminal voltage reaches zero. Both models behave similarly at normal operation (e.g., 1C). However, at high C-rates (e.g., >50C) , significant differences in terminal voltage emerge between the models: the SPMe voltage reaches 0V faster than the EqCM, which can be explained by local Li concentration depletion and saturation [39], factors that are not captured in the EqCM. Additionally, the EqCM, underestimates the battery temperature by up to 20°C and the total pressure by up to 30 kPa. These modeling errors motivate the need for the robust enforcement of safety constraints capable of coping with uncertainty in the EqCM; this challenge will be addressed in the next section.

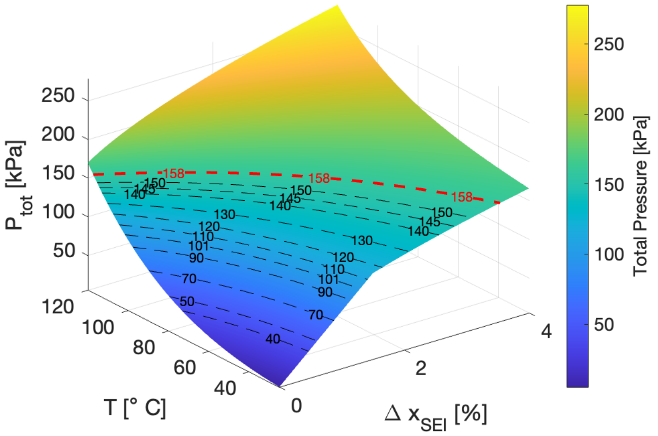

Figure 5: 3D visualization of the cell gas pressure as a function of temperature and normalized x_{SEI} decomposition ($\frac{\Delta x_{\text{SEI}}}{x_{\text{SEI},0}}$). Iso-pressure lines are marked with dashed lines and values. The maximum pressure (before venting) is represented in dashed red line.

3.3. Iso-Pressure Maps

The total pressure, expressed as a function of Δx_{SEI} and cell temperature T, $P_{tot} = h_p(T, \Delta x_{\text{SEI}})$, is detailed through equations (6)-(12). Figure 5 and 6 illustrate the impact of the states Δx_{SEI} and T on the total pressure. One can observe that an increase in T and/or Δx_{SEI} results in a (nonlinear) rise in total pressure. To prevent venting, the total pressure must remain below the threshold P_{max}, which can be determined experimentally as discussed in [40, 15]. We introduce the following

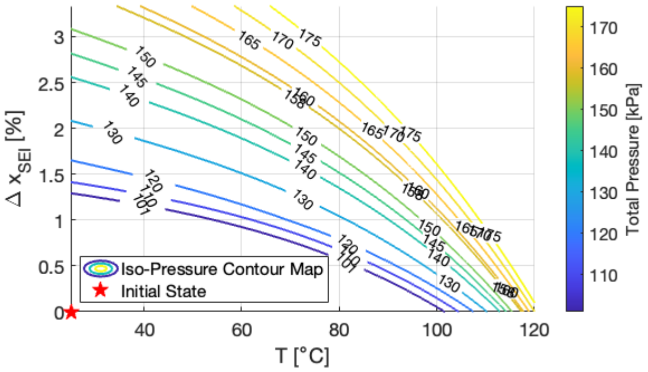

Figure 6: Iso-Pressure contours with the initial $(T, \Delta x_{\text{SEI}})$ state shown in red star, and the percentage of the SEI decomposition, normalized as $\frac{\Delta x_{\text{SEI}}}{x_{\text{SEI},0}}$.

Boolean indicator to indicate the venting condition:

$$\gamma_{vent}(P_{tot}(T, \Delta x_{\text{SEI}})) = \begin{cases} 0 & P_{tot} < P_{max} \\ 1 & \text{otherwise} \end{cases} . \tag{13}$$

It is interesting to note that this indicator separates the space $(T, \Delta x_{\text{SEI}})$ into two regions of: i) a safe pressure domain and ii) an unsafe pressure operating domain (see Figure 7). Our objective is to remain in the safe domain, where $\gamma_{vent}(P_{tot}) = 0$.

3.4. *Safety Constraints*

In addition to the pressure constraint, we also need to enforce temperature and SoC limits:

$$T(t) \leq T_{max}, \tag{14a}$$
$$SoC_{min} \leq SoC(t), \tag{14b}$$
$$P_{tot}(T(t), \Delta x_{\text{SEI}}(t)) \leq P_{max}, \tag{14c}$$

where the sub-script *min* defines the minimum allowed quantity and *max* the maximum. The upper limit on temperature (14a) is imposed to ensure thermal safety of the cell, while a lower bound on the SoC (14b) is enforced to prevent over-discharge, which can result in copper dissolution [43], internal short-circuiting, or irreversible capacity loss [44]. Finally, the gas pressure (P_{tot}) is constrained to prevent cell venting, which may be triggered by excessive gas generation from electrolyte decomposition or unwanted side reactions, particularly during emergency discharge events. This limit is especially critical in battery cells that do not contain pressure-relief valves, such as pouch cells.

In addition, the battery discharge current should also be constrained:

$$0 \leq I(t) \leq I_{max}, \tag{15}$$

where I_{max} is the maximum current allowed by the discharge device.

4. Control Design

Our objective is to design a control method that computes a discharging current $u = I(t)$ that:

Table 1: State-Space and Nonlinear Model Functions.

Matrix / Function	**Definition**
$A,\ B$	$A = \begin{bmatrix} 0 & 0 \\ 0 & -\frac{1}{R_1 C_1} \end{bmatrix}, \quad B = \begin{bmatrix} -\frac{1}{Q} \\ \frac{1}{C_1} \end{bmatrix}$
$f(x)$	$\begin{bmatrix} -\frac{hA_{\text{surf}}(x_1 - T_{amb})}{m_{cell}C_p} \\ A_{\text{SEI}} x_{\text{SEI},0} \exp\left(-\frac{E_{\text{SEI}}}{k_b x_1}\right) \end{bmatrix}$
$g_1(z),\ g_2$	$g_1(z) = \begin{bmatrix} \frac{z_2}{m_{cell}C_p} \\ 0 \end{bmatrix}, \quad g_2 = \begin{bmatrix} \frac{R_s}{m_{cell}C_p} \\ 0 \end{bmatrix}$

(i) robustly enforces the safety constraints (14) and the input constraint (15), despite parametric uncertainties and unmodeled dynamics in the EqCM, as discussed in Section 3.2;

(ii) is as close as possible to the reference discharge current $I^{\star}_{disch}$.

To facilitate the control design it is useful to partition the battery model into two sub-systems: i) the electrical sub-system with states $z = [SoC, V_1]^{\top}$ and ii) the temperature-SEI subsystem with states $x = [T, \Delta x_{\text{SEI}}]^{\top}$ and pressure output $y = P_{tot}$ (see (6)-(12)). This leads to the following partitioned state-space model:

$$\dot{z} = Az + Bu = f_z(z, u), \tag{16a}$$
$$\dot{x} = f(x) + g_1(z)u + g_2 u^2 = f_x(x, z, u), \tag{16b}$$
$$y = h_p(x), \tag{16c}$$

where the matrices A, B are obtained from (2), $f(\cdot)$, $g_1(\cdot)$, and g_2 are derived from (4) and (9b), and h_p encompasses (6)-(11). These matrices and functions are summarized in Table 1, and their local Lipschitz continuity is established in Appendix B.

The safety constraints (14) can be encoded via the sets:

$$\mathcal{X} = \{x = [T, \Delta x_{\text{SEI}}]^{\top} : T \leq T_{max}\}, \tag{17}$$
$$\mathcal{Z} = \{z = [SoC, V_1]^{\top} : SoC_{min} \leq SoC\}, \tag{18}$$
$$\mathcal{Y} = \{y : y = h_P(x) \leq P_{max}\}, \tag{19}$$

while the input constraint is formalized as:

$$\mathcal{U} = \{u \in \mathrm{R} : u \leq I_{max}\}. \tag{20}$$

In this section, the states x and z are assumed to be available for feedback. The design and implementation of the state observer used to estimate these variables are detailed in Section 5.

4.1. *Approximation of the Pressure Safe-Set*

The direct enforcement of the safe pressure set $\mathcal{Y}$ is challenging due to the non-linear algebraic equation $h_P(x)$, which contains $\max(\cdot)$ operations. To facilitate control design, we map $\mathcal{Y}$ into the temperature-SEI space, i.e.:

$$\mathcal{X}_{P,safe} = \{x \in \mathcal{X} : h_P(x) \in \mathcal{Y}\} \tag{21}$$

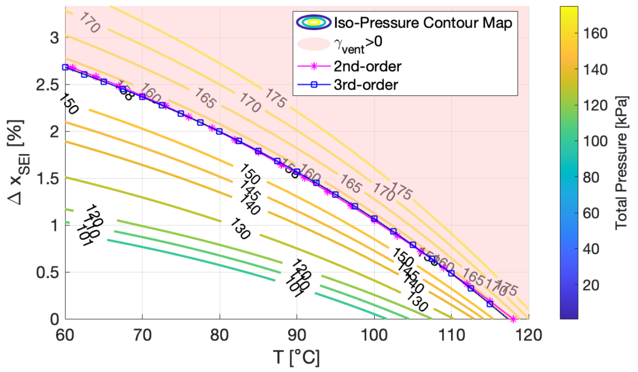

Figure 7: Iso-pressure contour map in the $(T, \Delta x_{\text{SEI}})$ space. The plot also shows the polynomial approximations (second and third order) of the pressure-safe border, and the unsafe region ($\gamma_{vent} > 0$).

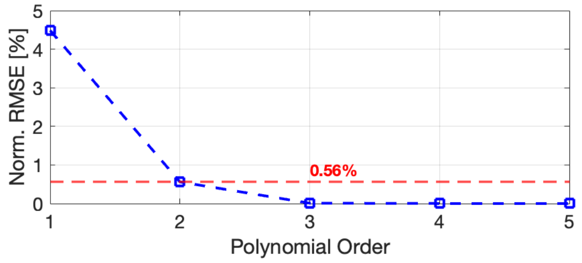

Figure 8: Normalized Root Mean Square Error (RMSE) of approximating the border of safe set $\mathcal{X}_{P,safe}$ with a polynomial $p^\top \phi(T)$. The horizontal axis represents the order of the polynomial approximation. Vertical axis depicts normalized RMSE, computed as $100 \times \frac{\sqrt{E(\phi)}}{\max_k \Delta x_{\text{SEI},k}}$, where the denominator contains the maximum value of Δx_{SEI} along the border $\mathcal{X}_{P,safe}$. The red dashed line highlight the error for the 2nd-order polynomial.

Figure 7 provides a graphical representation of this safe pressure set, obtained through discretization of $\mathcal{X}$. It is interesting to note that $\mathcal{X}_{P,safe}$ can be approximated with good accuracy using the super-level of a polynomial function in T:

$$\hat{\mathcal{X}}_{P,safe} = \{x = [T, \Delta x_{\text{SEI}}]^\top \in \mathcal{X} : \Delta x_{\text{SEI}} \leq \Delta x_{\text{SEI}}^{n,max}(T)\} \tag{22}$$

where $\Delta x_{\text{SEI}}^{n,max}(T) = p^\top \phi(T)$ is a polynomial function of order n with basis functions $\phi(T) = \begin{bmatrix} 1 & T & T^2 & \dots & T^n \end{bmatrix}^\top$ and parameters $p = \begin{bmatrix} p_0 & p_1 & \dots & p_n \end{bmatrix}^\top$.

The coefficients p_j, can be determined by solving the following least-squares problem:

$$\min_p \frac{1}{N_p} \sum_{k=1}^{N_p} (\Delta x_{\text{SEI},k} - p^\top \phi(T_k)))^2 = E(\phi), \tag{23}$$

where $(T_k, \Delta x_{\text{SEI},k})$ represents sample from the border of $\mathcal{X}_{P,safe}$, and N_p is the number of samples. Figure 7 shows polynomial approximations of orders $n = 2$, and 3, while Figure 8 depicts the normalized RMSE for this fitting problem. A first-order polynomial yields a fitting error of 4.5%. Increasing the order to 2, decreases the fitting error to 0.56%. Higher-order polynomials (3rd–5th) do not yield substantial improvements, but increase complexity. Therefore, we selected the third order polynomial as a balance between accuracy and simplicity.

The polynomial approximation $\hat{\mathcal{X}}_{P,safe}$ provides a more tractable formulation for control design, avoiding the complexities associated with the more complex and nonlinear $\mathcal{X}_{P,safe}$.

4.2. Safety Sets and Control Barrier Function

This section describes how CBF are used to enforce the safe sets $\mathcal{X}, \mathcal{Z}, \hat{\mathcal{X}}_{P,safe}$ As the first design step , we reformulate the individual safety constraints as super-level sets of a differentiable function $c_i(.)$:

$$C_1 = \{(z, x) : c_1(z) = SoC - SoC_{min} \geq 0\}, \tag{24a}$$
$$C_2 = \{(z, x) : c_2(x) = T_{max} - T \geq 0\}, \tag{24b}$$
$$C_3 = \{(z, x) : c_3(x) = \Delta x_{\text{SEI}}^{n,max}(T) - \Delta x_{\text{SEI}} \geq 0\}. \tag{24c}$$

We say that the battery is safe if the state trajectory is kept within the safety set $(z(t), x(t)) \in C = C_1 \cap C_2 \cap C_3$. Formally, this implies that C is forward invariant:

Definition 1. *([17]) A set C is forward invariant if $x(t) \in C$ for all $t \geq 0$ and all $x(0) \in \mathcal{X}$.*

The second step consists of deriving sufficient conditions on the control input u to enforce the invariance of the set C, i.e., to ensure that the functions $c_i(\cdot)$ remain positive. The core principle of CBF is to limit the rate of change of c_i, preventing c_i from transitioning to (unsafe) negative values. If c_i has relative degree one [17], this can be enforced by choosing $u \in \mathcal{U}$ such that:

$$\dot{c}_i(x, z, u) \geq -\alpha_i(c_i(x, z)), \quad \forall i = \{1, 2, 3\} \tag{25}$$

where $\alpha_i(\cdot)$ is an extended class $\mathcal{K}$ function ($\mathcal{K}_\infty^e$) according to Definition 2.

Definition 2. *([17]) A continuous function $\alpha(\cdot) : \mathbb{R} \to \mathbb{R}$ is an extended class $\mathcal{K}$ function if*

(i) $\alpha(0) = 0$;

(ii) $\alpha(\cdot)$ *is strictly increasing;*

(iii) $\lim_{r\to\infty} \alpha(r) = \infty$ *and* $\lim_{r\to-\infty} \alpha(r) = -\infty$.

For simplicity, this work considers linear functions $\alpha_i(\zeta) = K_i\zeta$, with K_i serving as tuning parameters. Expanding the inequalities (25) with the safety sets defined in (24) leads to the following conditions on the control input:

$$\begin{aligned}
\mathcal{U}_C(x, z) &= \{u \in \mathcal{U} : \\
\dot{c}_1(z, u) &= -\frac{u}{Q} \geq -\alpha_1(c_1(z)), && (26) \\
\dot{c}_2(x, z, u) &= -\frac{R_s u^2 + V_1 u - hA_{\text{surf}}(T - T_{amb})}{m_{cell} C_p} \\
&\geq -\alpha_2(c_2(x)), && (27) \\
\dot{c}_3(x, z, u) &= \frac{\partial \Delta x_{\text{SEI}}^{n,max}(T)}{\partial T} \dot{T} - \Delta \dot{x}_{\text{SEI}} \\
&= \frac{R_s u^2 + V_1 u}{m_{cell} C_p} \frac{\partial \Delta x_{\text{SEI}}^{n,max}(T)}{\partial T} \\
&\quad - \frac{hA_{\text{surf}}(T - T_{amb})}{m_{cell} C_p} \frac{\partial \Delta x_{\text{SEI}}^{n,max}(T)}{\partial T} \\
&\quad - A_{\text{SEI}} x_{\text{SEI},0} \exp\left(-\frac{E_{\text{SEI}}}{k_b T(t)}\right) \\
&\geq -\alpha_3(c_3(x))\}. && (28)
\end{aligned}$$

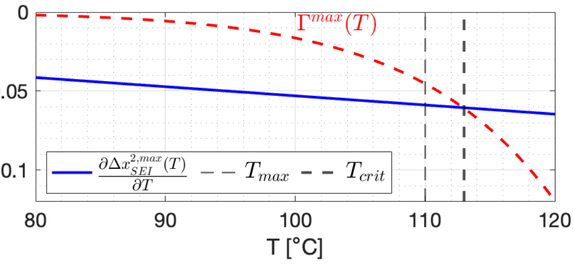

Figure 9: Graphical representation of the condition (ii) of Theorem 1 for the second-order polynomial $\Delta x^{2,max}_{\text{SEI}}(T)$, and the maximum bound ($\Gamma^{max}(T)$), in dashed red line.

The set $\mathcal{U}_C(x,z)$ may offer multiple (safe) control actions for a given state (x,z). An optimization-based approach is employed to select the control action. The objective is to find a control input u that satisfies $\mathcal{U}_C(\cdot)$ while minimizing the deviation from the to reference discharge current $I^\star_{disch}$. The final control input can be obtained by solving the following optimization problem

$$u^\star(z,x) = \arg \min_{u \in \mathcal{U}_C(z,x)} \|u - I^\star_{disch}\|_2^2. \tag{29}$$

4.3. Numerical Feasibility and Convexity

If $\mathcal{U}_C(x,z) = \emptyset$, then the previous problem lack a feasible solution. In practice, it is important to understand the conditions for numerical feasibility. The following result shows that if the (temperature) derivative of the polynomial approximation $\Delta x^{n,max}_{\text{SEI}}(T)$ is upper bounded by a temperature-dependent function ($\Gamma^{max}(T)$) then $\mathcal{U}_C(x,z) \neq \emptyset$ and the optimization problem remains feasible.

Theorem 1. *Assume that the following inequalities hold:*

(i) $T > T_{amb}$*,*

(ii) $\frac{\partial \Delta x^{n,max}_{SEI}(T)}{\partial T} \leq -k_f \frac{\exp\left(-\frac{E_{SEI}}{k_b T}\right)}{T - T_{amb}} = \Gamma^{max}(T)$*,*

for every $(z,x) \in C$*, where* $x = [T, \Delta x_{SEI}]^\top$*, and* $k_f = \frac{m_{cell} C_p A_{SEI} x_{SEI,0}}{h A_{surf}}$*. Then* $\mathcal{U}_C(z,x) \neq \emptyset$ *and the optimization problem (29) is feasible for every* $(z,x) \in C$*.*

Proof. This proof consists in demonstrating demonstrating that conditions (26), (27) and (28) are fulfilled for the candidate $u = 0$. As a result, $0 \in \mathcal{U}_c(z,x) \neq \emptyset$. See Appendix C for a detailed proof. ☐

Figure 9 shows that $\frac{\partial \Delta x^{n,max}_{\text{SEI}}(T)}{\partial T}$ satisfies the upper bound $\Gamma^{max}(T)$ defined in Theorem 1 for the EqCM parameters listed in Table 4. For temperatures above $T_{crit} \approx 113°C$, where condition (ii) is no longer satisfied, slack variables must be included in the optimization problem to preserve numerical feasibility.

Lemma 1. *Consider the safe set C and the system (16). Assume the safe input set is not empty,* $\mathcal{U}_C(z,x) \neq \emptyset$*,* $\forall (z,x) \in C$*. Then, any Lipschitz continuous controller* $u(z,x)$ *such that* $u(z,x) \in \mathcal{U}_C(z,x)$*,* $\forall (z,x) \in C$ *will render the set C forward invariant. [17]*

Proof. This Lemma is an extension from [17, Proposition 2 and Corollary 2]. The only small difference is the non-affine structure of (16), which contains the quadratic input term u^2 in the x dynamics. This means we need to check that $f_x(w, u(w))$, $w = [z^\top, x^\top]^\top$ is Lipschitz continuous. This can be verified by inspecting the gradient $\frac{\partial f_x}{\partial w}$:

$$\frac{\partial f_x}{\partial w} = \frac{\partial f}{\partial w} + \frac{\partial g_1}{\partial w} u + g_1 \frac{\partial u}{\partial w} + \frac{\partial g_2}{\partial w} u^2 + g_2 2u \frac{\partial u}{\partial w}. \tag{30}$$

Since we assumed that f, g_1, g_2, u are locally Lipschitz, the terms $\frac{\partial f}{\partial w}$, $\frac{\partial g_1}{\partial w}$, $\frac{\partial g_2}{\partial w}$, and $\frac{\partial u}{\partial w}$ are bounded. The control action $u \in \mathcal{U}$ is also bounded. This means that $\frac{\partial f_x}{\partial w}$ is bounded and is Lipschitz continuous [45, Chap. 3]. ☐

Lemma 2. *The optimization problem (29) is convex.*

The detailed proof of this lemma is provided in Appendix D, where we establish convexity by analyzing the structure of the cost function and the constraint functions.

4.4. Robust CBF

In this section, we develop a robust CBF formulation to account for disturbances, such as estimation errors and unmodeled effects. To simplify the discussion, consider the x dynamics (16b) subject to an additive disturbance:

$$\dot{x} = f(x) + g_1(z)u + g_2 u^2 + g_d(x,z)d, \tag{31}$$

where $d \in \mathcal{D} \subset \mathcal{R}$ is a bounded disturbance and $g_d(x,z)$ is a known function, possibly dependent on (x,z). The term $g_d(x,z)d$ captures the influence of unmodeled n effects (see Section 3.2). In the thermal domain, this may include unexpected heat generation due to contact resistance or local hotspots, fluctuations in ambient conditions and inaccuracies in thermal modeling. In the context of SEI decomposition, it may also represent side reactions or estimation errors that are not explicitly included in the nominal model.

The safety conditions (27) and (28) under additive disturbances are revised as follows:

$$\frac{\partial}{\partial t} c_i(x) + \alpha(c_i(x)) \geq 0, \tag{32a}$$

$$\underbrace{\frac{\partial c_i}{\partial x}\left(f(x) + g_1(z)u + g_2 u^2\right)}_{\dot{c}_i^{nom}(x,z,u)} + \underbrace{\frac{\partial c_i}{\partial x} g_d(x,z)d}_{\rho_i(x,z,d)} + \alpha(c_i(x)) \geq 0, \tag{32b}$$

$$\dot{c}_i^{nom}(x,z,u) + \rho_i(x,z,d) + \alpha(c_i(x)) \geq 0. \tag{32c}$$

The last equation splits $\frac{\partial}{\partial t} c_i(x)$ into two terms: i) $\dot{c}_i^{nom}$, the nominal term; and ii) $\rho_i(x,z,d)$, which captures the impact of the disturbance on the CBF safety condition.

Assume that we can compute the "worst-case" disturbance, i.e., the value of d that minimizes the left side of the previous inequality:

$$\underline{\rho}_i = \min_{x \in \mathcal{X}, z \in \mathcal{Z}, d \in \mathcal{D}} \rho_i(x,z,d). \tag{33}$$

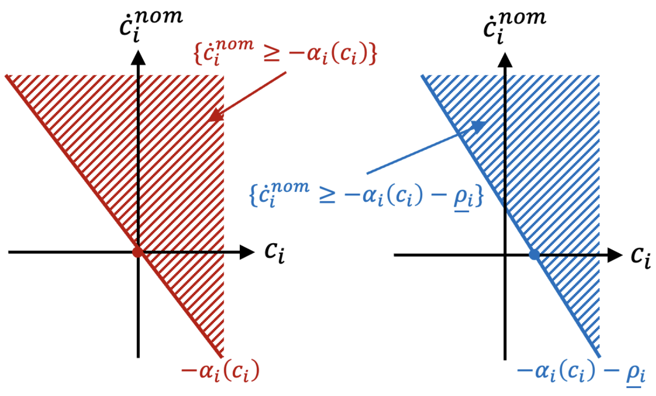

(a) (b)

Figure 10: a) Nominal CBF, b) Robust CBF (assuming $\underline{\rho}_i < 0$).

Appendix E details how to determine $\underline{\rho}_i$ when the battery model is subject to parameter uncertainties. Typically, $\underline{\rho}_i < 0$. Consider the following sequence of inequalities:

$$\begin{aligned}\dot{c}_i^{nom}(x,z,u) + \rho_i(x,z,d) + \alpha(c_i(z)) \geq \\ \dot{c}_i^{nom}(x,z,u) + \underline{\rho}_i + \alpha(c_i(z)) \geq 0.\end{aligned} \tag{34}$$

The first inequality is fulfilled by the definition of $\underline{\rho}_i$. If the second holds, the CBF is robust against bounded additive disturbances. The second inequality can be rewritten as:

$$\dot{c}_i^{nom}(x,z,u) \geq -\alpha(c_i(z)) - \underline{\rho}_i. \tag{35}$$

If $\underline{\rho}_i = 0$, then the original CBF inequalities (27) and (28) are recovered. If $\underline{\rho}_i < 0$, then the constraint is "tightened" to account for the potential (worst-case) impact of the disturbance. From a practical perspective, this tightening will introduce a *safety margin*, preventing the system from operating near the boundary of the safety set. This concept is illustrated in Figure 10: when c_i approaches zero, inequality (35) forces $\dot{c}$ to be positive, even when the system is still inside the safety set ($c_i > 0$). To prevent potential numerical infeasibility caused by constraint tightening a slack variable s_i is introduced:

$$\dot{c}_i^{nom}(x,z,u) \geq -\alpha(c_i(z)) - \underline{\rho}_i - s_i, \quad s_i \geq 0. \tag{36}$$

The resulting robust CBF problem can be formulated as:

$$\begin{aligned} u^\star = \arg\min_u \quad & \left\|u - I_{disch}^\star\right\|_2^2 + \sum_i \gamma_i s_i^2 && \text{(37a)}\\ \text{s.t.} \quad & u \in \mathcal{U}, && \text{(37b)}\\ & \dot{c}_i^{nom}(x,z,u) \geq -\alpha(c_i(z)) - \underline{\rho}_i - s_i, && \text{(37c)}\\ & s_i \geq 0 && \text{(37d)}\end{aligned}$$

where γ_i represents the weight penalizing the relaxation of the CBF condition.

Remark: Under suitable assumptions, state estimation errors—which may be introduced by the Observer described in the next section—can be treated as additive disturbances Let the true state $x = \begin{bmatrix} T & \Delta x_{\mathrm{SEI}} \end{bmatrix}^\top$ be subject to a bounded additive perturbation[1]:

$$x = \hat{x} + \epsilon_x, \quad \|\epsilon_x\| \leq \bar{\epsilon}_x, \tag{38}$$

where $\hat{x}$ is the estimated state, ϵ_x captures the estimation error and $\bar{\epsilon}_x$ is the error bound. Substituting (38) in (16b) we obtain the state dynamics

$$\dot{\hat{x}} + \dot{\epsilon}_x = f(\hat{x} + \epsilon_x) + g_1(z)u + g_2 u^2, \tag{39}$$

which can be re-written as

$$\dot{\hat{x}} = f(\hat{x}) + g_1(z)u + g_2 u^2 + \underbrace{I}_{g_d}\underbrace{f(\hat{x} + \epsilon_x) - f(\hat{x}) - \dot{\epsilon}_x}_{d_o}, \tag{40}$$

where d_o is the additive disturbance due to estimation error and g_d is the identity matrix. To apply the robust CBF described in this section, the additive disturbance d_o needs to be bounded. Recall that the function $f(x)$ is Lipschitz (see Lemma 1). As a result, there exists a constant L_f such that

$$\|f(\hat{x} + \epsilon_x) - f(\hat{x})\| \leq L_f \|\epsilon_x\| \leq L_f \bar{\epsilon}_x. \tag{41}$$

Assuming $\dot{\epsilon}_x$ is bounded, $\|\dot{\epsilon}_x\| \leq \bar{\dot{\epsilon}}_x$, then the upper bound on the disturbance is defined as

$$\|d_o\| \leq L_f \bar{\epsilon}_x + \bar{\dot{\epsilon}}_x. \tag{42}$$

This bound can then be used to tune the parameter $\underline{\rho}_i$ of the robust CBF when the estimate $\hat{x}$ is used instead of x. In addition to estimation errors, the model may also be affected by parametric uncertainties. We refer the reader to Appendix E for a discussion how on to formulate and bound the additive disturbance d in the presence of uncertainties in the model parameters.

5. Observer Design and Analysis

The CBF solution $u^\star$ in (37) depends on the state vectors $x = [T, \Delta x_{\mathrm{SEI}}]^\top$ and $z = [\mathrm{SoC}, V_1]^\top$. In practice, several of these states—most notably the SEI layer decomposition Δx_{SEI}—cannot be directly measured. To overcome this limitation, we develop a virtual sensing to estimate x, z based on non-invasive sensing. Our approach assumes that the following (extended) measurements are available:

$$\tilde{y} = \begin{bmatrix} V_t & T & \Delta\sigma \end{bmatrix}^\top, \tag{43}$$

which include the surface temperature T, battery terminal voltage V_t, and compressive stress $\Delta\sigma$ (for details on the compression stress sensor, see [40] and Figure 1). The inclusion of pressure measurements is crucial for the estimation of Δx_{SEI}, which is otherwise unobservable. Additionally, we define an extended state vector w that concatenates the electrical, thermal, and SEI states:

$$w = \begin{bmatrix} \mathrm{SoC} & V_1 & T & \Delta x_{\mathrm{SEI}} \end{bmatrix}^\top. \tag{44}$$

---

[1] a similar analysis can be performed for uncertainties in the z estimation, which is omitted here to preserve conciseness

The extended state dynamics can be rewritten as

$$\begin{bmatrix} S\dot{o}C \\ \dot{V}_1 \\ \dot{T} \\ \Delta\dot{x}_{\text{SEI}} \end{bmatrix} = \begin{bmatrix} \dot{w}_1 \\ \dot{w}_2 \\ \dot{w}_3 \\ \dot{w}_4 \end{bmatrix} = \begin{bmatrix} -\frac{u}{Q} \\ -\frac{w_2}{R_1C_1} + \frac{u}{C_1} \\ \frac{R_su^2+w_2u-hA_{\text{surf}}(w_3-T_{amb})}{m_{cell}C_p} \\ A_{\text{SEI}}x_{\text{SEI},0}\exp\left(-\frac{E_{\text{SEI}}}{k_bw_3}\right) \end{bmatrix}, \tag{45}$$

and the outputs equations are defined as

$$\begin{aligned} \tilde{y} = h(w,u) &= \begin{bmatrix} V_{ocv}(w_1) - R_su - w_2 \\ w_3 \\ \Delta\sigma \end{bmatrix}, \\ &\approx \begin{bmatrix} V_{ocv}(w_1) - R_su - w_2 \\ w_3 \\ P_{tot}(w_3,w_4) - \sigma_0 - P_{atm} \end{bmatrix}. \end{aligned} \tag{46}$$

The final equality assumes that $\Delta\sigma$ is dominated by gas pressure during emergency discharge, i.e.,

$$P_{\text{tot}}(w_3,w_4) - \sigma_0 - P_{\text{atm}} \geq \frac{E\alpha_{\text{cell}}\Delta T}{L}. \tag{47}$$

5.1. Observability Analysis

Before designing an observer for the state w, it is important to understand the observability of the nonlinear state model (45), (46). More specifically, we must determine if the state w can be reconstructed from the extended measurement $\tilde{y}$ and the model (45), (46) . The following result addresses this question via a linear analysis:

Proposition 1. *The battery system* (45)*,* (46) *is locally observable.*

Proof. Consider the system linearized around a nominal operating point $(w^\star, u^\star)$. Defining the perturbations $\Delta w = w - w^\star$, $\Delta u = u - u^\star$, the local state and output dynamics are given by

$$\Delta\dot{w} = A\big|_{w^\star,u^\star}\Delta w + B\big|_{w^\star,u^\star}\Delta u, \tag{48a}$$

$$\Delta\tilde{y} = C\big|_{w^\star}\Delta w. \tag{48b}$$

The Jacobian matrices and output sensitivities required for the observability analysis are summarized in Table 2. The third output equation depends on the temperature and gas-generation states through the sensitivities c_{33} and c_{34}, which are also listed in Table 2.

The observability matrix for this linearized model is given by:

$$O = \begin{bmatrix} C^\top & (CA)^\top & (CA^2)^\top & (CA^3)^\top \end{bmatrix}^\top, \tag{49}$$

Recall that the system is (locally) observable if the observability matrix is full rank ($\text{rank}(O) = 4$). Verifying this condition analytically is not easy. Instead, we rely on numerical methods to check the rank condition. This evaluation is performed over a grid of operating points to account for the system's nonlinear behavior. Specifically, the input $u^\star$ was chosen as a constant discharge current, $u^\star_j = j$ C-rate, where $j \in \{1,\ldots,90\}$ is the applied C-rate. For each j, the state trajectories $w^\star_j, \tilde{y}^\star_j$ were computed in discrete time using the forward Euler method with a sampling time of 0.5s and an initial state of

$$w_0 = \begin{bmatrix} 1 & 0.1 & 298.15 & 0 \end{bmatrix}^\top.$$

Across all tested operating points (j), the observability matrix maintained full rank ($\text{rank}(O) = 4$), confirming that the system is locally observable throughout the discharge operating range. □

Table 2: Linearized Model Matrices and Output Jacobians used for Observability Analysis.

Matrix / Term	**Definition**
$A\big\|_{w^\star,u^\star}$	$\begin{bmatrix} 0 & 0 & 0 & 0 \\ 0 & -\frac{1}{R_1C_1} & 0 & 0 \\ 0 & \frac{u^\star}{C_pm_{cell}} & -\frac{A_{\text{surf}}h}{C_pm_{cell}} & 0 \\ 0 & 0 & a_{43} & 0 \end{bmatrix}$
$B\big\|_{w^\star,u^\star}$	$\begin{bmatrix} -\frac{1}{Q} & \frac{1}{C_1} & \frac{w_2^\star + 2R_su^\star}{C_pm_{cell}} & 0 \end{bmatrix}^\top$
$C\big\|_{w^\star}$	$\begin{bmatrix} \frac{dV_{ocv}}{dw_1}\big\|_{w^\star} & -1 & 0 & 0 \\ 0 & 0 & 1 & 0 \\ 0 & 0 & c_{33} & c_{34} \end{bmatrix}$
a_{43}	$\frac{E_{\text{SEI}}}{k_bw_3^{\star 2}}A_{\text{SEI}}x_{\text{SEI},0}\exp\left(-\frac{E_{\text{SEI}}}{k_bw_3^\star}\right)$
$\begin{bmatrix} c_{33} & c_{34} \end{bmatrix}$	$c_{33} = \sum_{i\in\{\text{EC,DMC}\}} \frac{y_iB_i\ln 10}{(C_i + w_3^\star)^2}10^{A_i+\frac{B_i}{C_i+w_3^\star}} + \frac{m_{an}w_4^\star R}{2M_{C_6}V_h}$, $c_{34} = \frac{m_{an}Rw_3^\star}{2M_{C_6}V_h}$

To complement the linearized observability analysis, we also apply the nonlinear observability test based on Lie derivatives, following the framework in [46]. The nonlinear observability matrix is constructed as:

$$O_{nonlin} = \frac{d}{dw}\begin{bmatrix} L_f^0(y) & L_f^1(y) & \cdots & L_f^{n-1}(y) \end{bmatrix}^\top_{w_0}, \tag{50}$$

where $L_f^k(y)$ denotes the k-th Lie derivative of $h(w,u)$ (see (46)) along the system dynamics $f(w,u)$ (see (45)). A sufficient condition for locally weakly observability is that the matrix $O_{nonlin}(w_0)$ possesses full column rank [47]. To assess the numerical robustness of the observability, we compute the condition number of the observability matrix. For a matrix $O \in \mathbb{R}^{m\times n}$, the condition number with respect to the 2-norm is defined as:

$$\mathcal{K}(O) = \frac{\sigma_{\max}(O)}{\sigma_{\min}(O)}, \tag{51}$$

where $\sigma_{\max}(O)$ and $\sigma_{\min}(O)$ are the largest and smallest nonzero singular values of O, respectively. A lower condition number implies a greater sensitivity of the output to changes in the state, which improves numerical stability during state estimation. In contrast, a high condition number amplifies the effects of noise and leads to ill-conditioning.

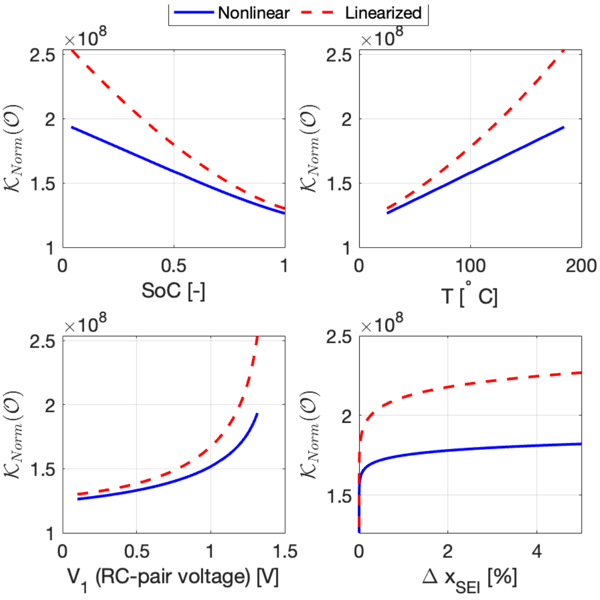

Figure 11: Normalized observability comparison of nonlinear (Lie derivative based) and linearized models evaluated at $(w^\star, u^\star = 40$ C-Rate) using rank and condition number metrics.

Figure 11 compares the *normalized* observability of the system evaluated through two different approaches: linearized observability at the operating point $(w^\star, u^\star)$ and nonlinear observability using the Lie derivative method. The normalization is performed as

$$K_{Norm} = \frac{K(O_{\{y=[V_t,T,P_{tot}]^\top\}})}{K(O_{\{y=w\}})}, \tag{52}$$

where $O_{\{y=w\}}$ is the observability matrix assuming all states w (44) are measurable. [48]

Although both methods produce full-rank observability matrices (rank(O)=rank(O_{nonlin}) = 4), the normalized condition number of the linearized observability matrix is higher than that of the nonlinear observability matrix. This implies that although the linearized system is theoretically observable, its sensitivity to state changes is reduced, and it is more prone to numerical instability during state estimation. Moreover, the normalized observability condition number is on the order of 10^8, indicating limited estimation accuracy. However, this magnitude remains comparable to those reported in similar battery works (e.g., see [46, 49]).

5.2. Extended Kalman Filter

After checking system observability, we can then construct an EKF to estimate the battery state w. We employ a discrete-time EKF, implemented using MATLAB's EKF block [50], and inspired from [51, 52]. The EKF recursively estimates the state vector based on the nonlinear state-space model (45) and the measurement model (46), where process and measurement noise are assumed to be zero-mean Gaussian with covariances $\tilde{Q} = \mathrm{diag}([\sigma_{w_1}, \sigma_{w_2}, \sigma_{w_3}, \sigma_{w_4}])$ and $\tilde{R} = \mathrm{diag}([\sigma_{y_1}, \sigma_{y_2}, \sigma_{y_3}])$, respectively, using the parameters reported in Table 5. The initial value of x_{SEI} is set to $x_{SEI,0}$ based on diagnostic data, which is assumed to be known *a priori*.

Table 3: Extended Kalman Filter Equations for the Battery System.

Step	**Equation**
State Prediction	$\hat{w}_{k\|k-1} = f(\hat{w}_{k-1}, u_{k-1})$
Error Covariance Prediction	$P_{k\|k-1} = A_{k-1}P_{k-1\|k-1}A_{k-1}^\top + \tilde{Q}_{k-1}$
Kalman Gain	$K_k = P_{k\|k-1}C_k^\top(C_kP_{k\|k-1}C_k^\top + \tilde{R}_k)^{-1}$
State Update	$\hat{w}_{k\|k} = \hat{w}_{k\|k-1} + K_k(y_k - h(\hat{w}_{k\|k-1}))$
Error Covariance Update	$P_{k\|k} = (I - K_kC_k)P_{k\|k-1}$

Table 4: Parameters of the EqCM used in the control design.

Parameter	**Symbol**	**Value**	**Unit**
Cell Capacity	Q	4.6	[Ah]
Cell Weight	m_{cell}	104	[g]
Negative Electrode Mass	m_{an}	19.107	[g]
Cell Cooling Area	A_{surf}	0.009	[m^2]
Internal Resistance	R_s	7.8	[mΩ]
RC Pair	R_1	7.5	[mΩ]
RC Pair	C_1	4.04	[kF]
Thermal Capacity	C_p	2108	[J/kgK]
Ambient Temperature	T_{amb}	25	[°C]
CHT[1] Coefficient	h	54.06	[W/Km^2]
Initial x_{SEI}	$x_{\text{SEI},0}$	0.15	[-]
SEI Decomposition F. F.[2]	A_{SEI}	2.20×10^{14}	[-]
SEI Decomposition A. E.[2]	E_{SEI}	2.24×10^{-19}	[J]

[1] CHT: Convective Heat Transfer

[2] F.F.: Frequency Factor, A. E.: Activation Energy

The EKF executes the recursive steps at each time step k as described in Table 3, where the Jacobians $A_k = \frac{\partial f}{\partial w}\Big|_{\hat{w}_{k-1},u_{k-1}}$ and $C_k = \frac{\partial h}{\partial w}\Big|_{\hat{w}_{k|k-1}}$ are evaluated at each step using the current state estimate. The functions $f(w,u)$ and $h(w)$ correspond to those in (45) and (46), respectively, and are discretized with the forward Euler method.

6. Numerical Results

In this section, we validate the performance of the CBF-based discharge controller using the high-fidelity model SPMe introduced in Section 3.2. The SPMe parameters were calibrated using experimental data from high-rate discharge tests (external short circuits), ensuring the model's validity for the emergency scenarios considered in this work (see Appendix A) for details. All parameters used are listed in Table 4 and Table 5. The simulations were carried out using

Table 5: CBF Controller, and EKF Parameter and Setpoints.

Parameter	**Symbol**	**Value**	**Unit**
CBF Linear Class-$\mathcal{K}$ Function Gains			
SoC CBF	K_Q	1	[-]
Temperature CBF	K_T	0.1	[-]
Pressure CBF	K_P	0.1	[-]
Setpoints			
Max. Discharging Current	I_{max}	414 (90C)	[A]
Max. Allowed Temp.	T_{max}	110	[°C]
Max. Prescribed Pressure	P_{max}	150	[kPa]
Minimum SoC	SoC_{min}	10	[%]
Additive Gaussian Measurement Noise Characteristics			
Terminal Voltage Var.	$\lvert e_{V_t}\rvert$	0.05	[V]
Temperature Var.	$\lvert e_T\rvert$	2	[°C]
Pressure Var.	$\lvert e_P\rvert$	1	[kPa]
Terminal Voltage Cov.	σ_{y_1}	10^{-5}	[V^2]
Temperature Cov.	σ_{y_2}	10^{-2}	[$\{°C\}^2$]
Pressure Cov.	σ_{y_3}	10^{-10}	[Pa^2]
Process Noise Cov.	σ_{w_1}	10^{-7}	[-]
Process Noise Cov.	σ_{w_2}	0.5	[V^2]
Process Noise Cov.	σ_{w_3}	10^{-3}	[$\{°C\}^2$]
Process Noise Cov.	σ_{w_4}	10^{-12}	[-]

MATLAB/Simulink Version R2024b[2]. The CBF optimization problems were formulated using *YALMIP* framework [53] and solved with the *interior-point nonlinear programming (ipopt)* solver [54]. A sampling period of $T_s = 0.5$s was employed for the simulations. The reference discharge current (1) was computed at the beginning of the simulation, and then held constant until the lower SoC limit was reached.

6.1. Benchmarking of Controllers (CBF vs PI vs MPC)

The first test, depicted in Figure 12, aims to discharge the battery cell within 40 s. This requires an aggressive current setpoint of $I^{\star}_{disch} = 90\,\text{C}$, which also corresponds to the maximum capacity of the discharge device ($I_{\max} = 90\,\text{C}$). The results show that the battery temperature increases rapidly at the beginning of the test, reaching the upper limit (110°C) in less than 10 s. To fulfill the temperature constraint, the CBF controller rapidly reduces the discharge current to approximately 10C. After 50s, the pressure constraint becomes dominant and the CBF controller adjusts the discharge current to remain within these *venting/pressure limits*. Due to the temperature and pressure constraints, it takes over 7 minutes to remove 70% of SoC, which is significant slower than the original (unfeasible) 40s of discharge time. Figure 13 illustrates the estimation performance of the EKF observer. The estimation accuracy is very high, with a peak error of less than 0.1%.

Table 6: Statistical comparison of per-iteration (per control update) computation time across 10 scenarios.

Control Method	**Mean** $[ms]$	**Std** $[ms]$	**Maximum** $[ms]$
MPC	297.85	221.81	3789.46
CBF-Based	16.33	4.60	207.93

To quantify performance benefits, we compare the proposed CBF controller against two baseline strategies: i) a PI controller designed to operate the battery at the temperature limit T_{max}, and ii) an MPC scheme that enforces, SoC, temperature and pressure constraints. The PI baseline controller was included to assess whether conventional temperature regulation (a common practice in the industry) is sufficient to indirectly limit battery pressure. Figure 12 shows that, although the PI controller regulates temperature effectively, the cell pressure exceeds the critical limit, which trigger a venting event.

The MPC scheme formulation follows our previous work in [16], with a control horizon of 20 steps and a sampling time of 0.5 seconds. To ensure a fair comparison, the MPC parameters were tuned to match the performance of the CBF-based controller, particularly in satisfying the safety constraints. We observed that the MPC with shorter horizons failed to enforce the safety constraints consistently. Figure 12 shows that both CBF and MPC schemes achieve comparable constraint satisfaction. However the CBF approach significantly outperforms MPC in terms of computational efficiency. As depicted in Figure 14, the average solver time for MPC is approximately 15 times higher than that of the CBF-based method. Table 6 provides a statistical summary over 10 scenarios with varying conditions[3]. The CBF-based method consistently demonstrates significantly lower computational demand, with a mean solver time of 16.33 ms (compared to 297.85 ms for MPC). This computational advantage makes the CBF formulation more attractive for real-time battery control applications on embedded systems.

6.2. Sensitivity and Robustness Analysis via Monte Carlo Simulations

Next, we evaluate the robustness of the CBF-based controller by introducing uncertainty into the model parameters. Let $\Delta = \begin{bmatrix}\theta_1 & \theta_2 & \dots & \theta_5\end{bmatrix}^\top \in \mathbb{R}^p$ denote the set of uncertain parameters (see Table 7). These parameters are assumed to be sampled from a stochastic distribution $\mathbb{B}$. To evaluate the safety of the CBF-based controller, we propose two performance metrics:

1. Maximum pressure violation (ψ): this measures the worst-case violation by computing the peak difference between

---

[2] All the simulations were performed on an Apple MacBook Pro with an M2 Pro chip and 16 GB of memory.

[3] where in each scenario, the model parameters Δ are sampled from the distribution $\mathbb{B}$; see Section 6.2 for details.

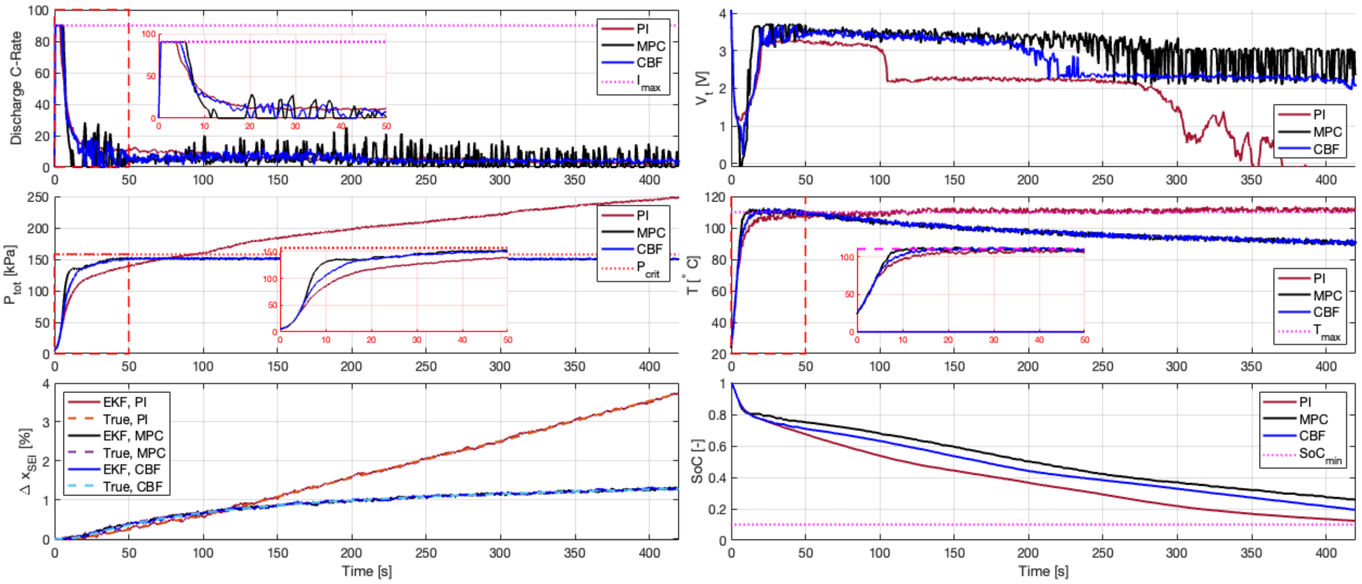

Figure 12: Simulation results of a fast battery discharge using the *nominal* CBF-based optimal controller applied to the high-fidelity SPMe model. The plot also includes baseline results obtained using an MPC controller, as well as a Proportional-Integral (PI) controller that only tracks the maximum temperature limit, for comparison.

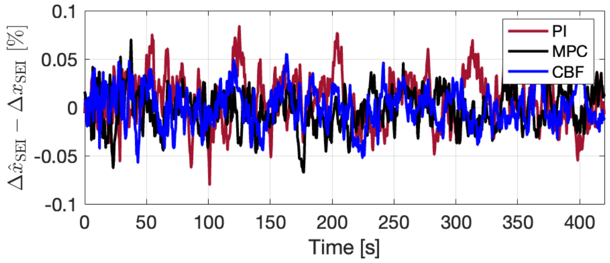

Figure 13: Estimation errors in Δx_{SEI} for the three discharge control strategies, illustrating the performance of the EKF.

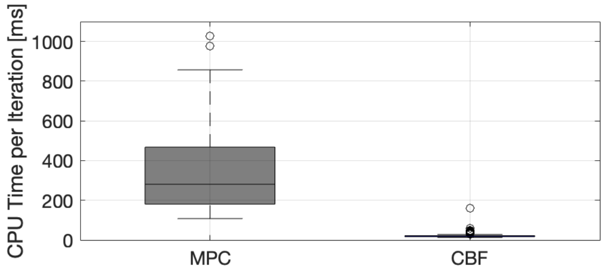

Figure 14: Comparison of solver computation time per iteration between MPC and CBF-based controllers. The box plot highlights the significantly lower and more consistent CPU time of the CBF approach. Outliers, marked as circles, indicate rare instances of longer solve times. (Results obtained with nominal battery model).

the cell pressure and the threshold P_{max}.

$$\psi(\Delta, \rho_i) = \max_t \left(P_{tot}(x(t,\Delta), \rho_i) - P_{max} \right). \tag{53}$$

If $\psi < 0$, then the system never violates the pressure constraint, and we are *safe*. If $\psi > 0$, pressure violation occurs.

2. Average pressure violation (ψ_{avg}): This metric captures the average pressure across N scenarios (sampled from $\Delta \sim \mathbb{B}$):

$$\psi_{avg}(\underline{\rho_i}) = \frac{\sum_j \psi(\Delta_j, \underline{\rho_i})}{N}, \tag{54}$$

where Δ_j is a sample from $\mathbb{B}$.

Note that since Δ is a random variable, ψ is also a random variable. In what follows,we assume that Δ is sampled from a uniform distribution with bounds defined in Table 7 . The selected ranges are intentionally conservative to account for worst-case scenarios; similar variation ranges for thermal parameters C_p and h have been used in [55], whereas our study adopts even broader ranges to further stress-test the system.

Case I: (Single-Parameter Uncertainty) Figure 15 shows the effect of varying individual parameters on the controller's safety performance. Among the five parameters, ambient temperature (T_{amb}) exhibits the largest impact on pressure violation, followed by the heat transfer coefficient (h). In contrast, the SEI frequency factor (A_{SEI}) has a comparatively smaller effects, indicating the controller's robustness to uncertainties in this parameter. Pressure constraint violations were observed across a wide range of parametric variations, highlighting the importance of robust control design.

Case II: (Multi-Parameter Uncertainty): Next, we extend the sensitivity study to investigate multiple simultaneous parameter uncertainties and evaluate the performance of robust CBF variants (with $|\underline{\rho_i}| > 0$). Figure 16 presents the results of a Monte Carlo simulation evaluating the maximum pressure constraint violation $\psi(\Delta, \underline{\rho_i})$ under parameter uncertainty, with 100 iterations performed for each test case. The plot compares the nominal CBF controller against four robust CBF variants with

Table 7: Controller Parameter Variation Range for Monte Carlo Simulations.

Param.	**Nom. Value**	**Unit**	**Range**	$\underline{\rho}_i$
$\theta_1 = A_{\mathrm{SEI}}$	0.2204×10^{15}	[-]	+50%	$-3.85e-11$
$\theta_2 = h$	54.06	[W/Km^2]	±45%	-0.085
$\theta_3 = C_p$	2108	[J/kgK]	±10%	-2.08
$\theta_4 = R_s$	0.0078	[Ω]	±30%	$-1.07e-5$
$\theta_5 = T_{amb}$	25	[°C]	±15%	-0.10

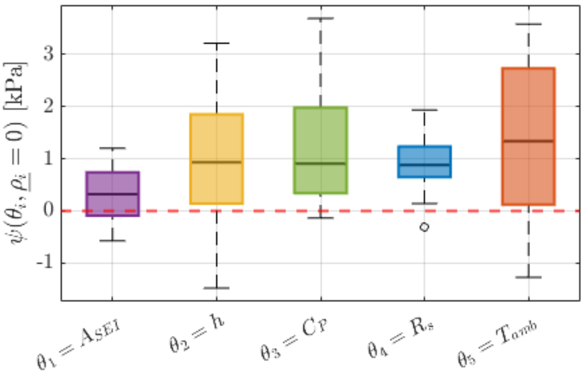

Figure 15: Effect of individual controller parameter uncertainty on pressure setpoint violation. For each parameter, 20 simulations were conducted across its uncertainty range (see Table 7) to quantify the impact on pressure regulation. This Figure shows the “box plot” of the variable $\psi(\theta_i)$. The central mark indicates the median value of ψ, while the bottom and top edges of the box indicate the 25th and 75th percentiles. The bottom and top bars indicate the minimum and maximum values of ψ.

increasing levels of robustness, parameterized by $\underline{\rho}_i$.

The nominal controller ($\underline{\rho}_i = 0$) exhibits the highest probability of constraint violations, indicating poor robustness to simultaneous parameter variations. In contrast, the robust controllers with higher $|\underline{\rho}_i|$ reduce the likelihood of pressure violations. As the robustness parameter $|\underline{\rho}_i|$ increases, the distribution shifts leftward, demonstrating improved safety margins for the robust CBF variants.

6.3. *Tuning of the Robust CBF Parameter $\underline{\rho}_i$*

An important practical question deals with the tuning of the parameter $\underline{\rho}_i$. This tuning can be performed in two ways. The first approach is analytical, and determines $\underline{\rho}_i$ by evaluating the worst-case value of the model parameters (see Appendix E for an example of this method, and numerical values reported in Table 7). The second approach leverages stochastic analysis. To explain this method, let us consider the expected value of the constraint violation indicator, denoted by $\mathbb{E}\big[\psi(\Delta,\underline{\rho}_i)\big]$. Assuming that Δ is sampled from the stochastic distribution $\mathbb{B}$, the value of $\underline{\rho}_i$ can be selected as the solution to the following optimization problem:

$$\underline{\rho}_i^{\star} = \arg \min_{\substack{\underline{\rho}_i\in\Gamma_i \\ \underline{\rho}_i\le 0,\ \mathbb{E}_{\Delta\sim\mathbb{B}}\left[\psi(\Delta,\underline{\rho}_i)\right]<0}} |\underline{\rho}_i| \tag{55}$$

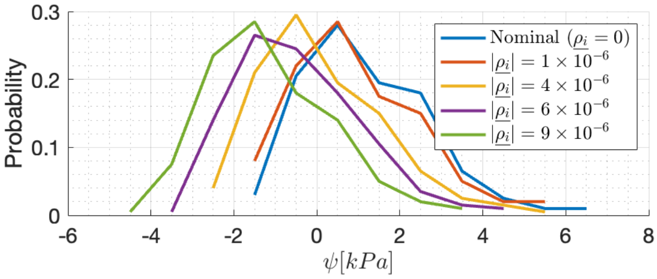

Figure 16: Monte Carlo simulation results showing the probability of pressure constraint violations ψ (see equation (53)) for the nominal ($\underline{\rho}_i = 0$), and robust controllers $\underline{\rho}_i$ for four cases.

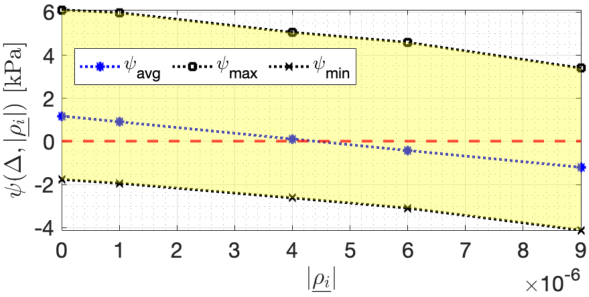

Figure 17: The average, minimum and maximum values of the constraint violation indicator $\psi(\Delta,\underline{\rho}_i)$ where the parameter vector Δ is sampled from a uniform stochastic distribution ($\Delta \sim \mathbb{B}$). The dashed red line indicates the limit for constraint violation (if $\psi > 0$ we have constraint violation) and the horizontal axis represents the bound $\underline{\rho}_i$.

where Γ_i denotes the admissible range of $\underline{\rho}_i$, and $\underline{\rho}_i^{\star}$ represents the smallest value of $|\underline{\rho}_i|$ (so that the CBF is not overly conservative) that robustly satisfies the pressure constraint.

Note that the above optimization problem involves only a single scalar decision variable, namely $\underline{\rho}_i$. As a result, it can be efficiently solved using gridding or other simple numerical methods. For example, Figure 17 illustrates the average value of ψ when Γ_i is discretized with a resolution of 1×10^{-6}. In this case selecting $|\underline{\rho}_i| \approx 4\times10^{-6}$ ensuring average pressure constraint satisfaction. Note that (55) can be adapted to account for alternative constraint satisfaction requirements, e.g. such as enforcing constraint fulfillment with a specified probability level (i.e., chance constraint optimization).

6.4. *Time-Domain Comparison of Nominal vs. Robust CBF*

Figure 18 compares the performance of the nominal and robust CBF controllers in two uncertain test scenarios involving uncertainty in Δ. Test 1 focuses on small parameter deviations (up to 4% deviation w.r.t. nominal values), while Test 2 introduces larger parameter variations (up to 60%) – see Table 8. All the other parameters are listed in Table 4 and Table 5. The results of Test 1 shows that the nominal CBF controller ($\underline{\rho}_i = 0$) maintains all safety limits without violation, whereas the robust controller behaves more conservatively by maintaining a ”safety marging” to the pressure limit, indicating reduced performance due to conservative robustness enforcement. In contrast, in Test 2, the nominal controller results in a violation of

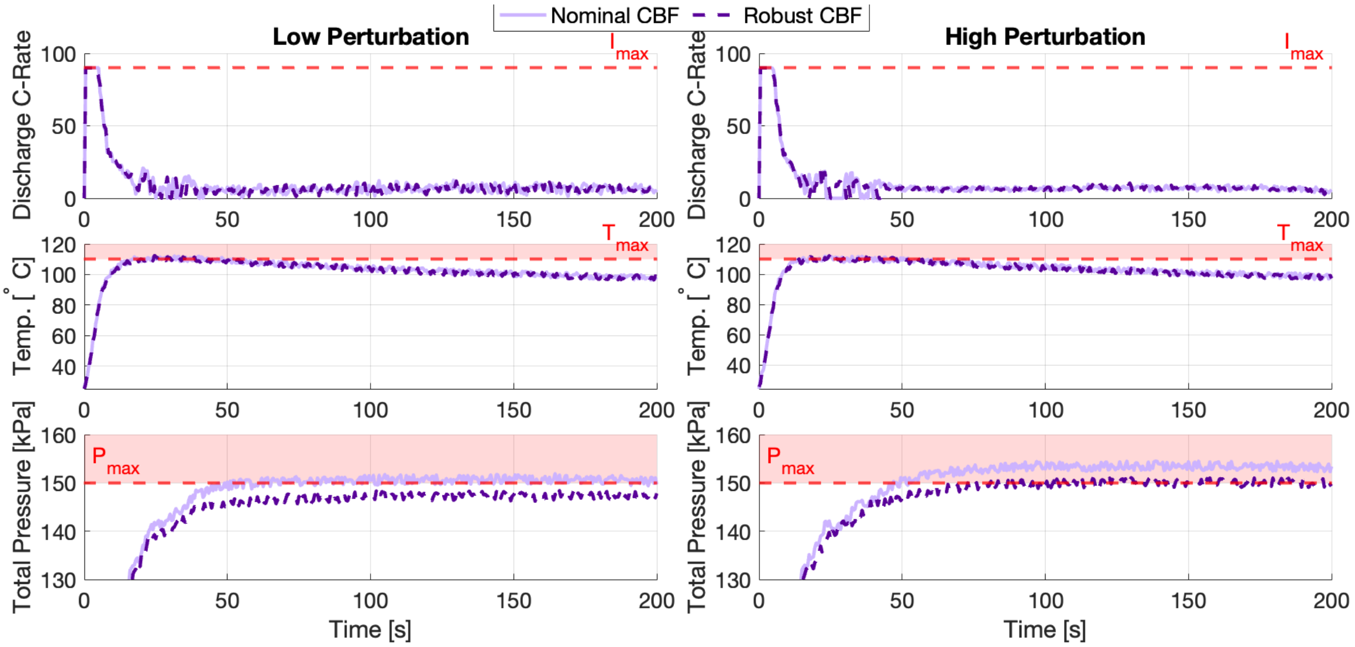

Figure 18: Comparison of nominal ($\underline{\rho_i} = 0$) and robust (with $|\underline{\rho_i}| = 0.9 \times 10^{-5}$) CBF strategies across two test scenarios involving stochastic selection of uncertain parameters. The left column corresponds to parameter vector $\underline{\Delta}$ from Test 1 (low parameter uncertainty) and the right column to Test 2 (high parameter uncertainty), as described in Table 8. The top rows show the discharge current normalized by capacity (C-rate), the middle rows the measured battery temperature, and bottom rows the total pressure (P_{tot}). Dashed red line indicates the maximum pressure limit.

Table 8: Uncertain parameter realizations of Test 1 and Test 2.

Parameter	Nom. Val.	Test 1	Test 2
$\theta_1 = A_{\mathrm{SEI}}/10^{15}$	0.2204 [-]	0.23 (+4%)	0.33 (+50%)
$\theta_2 = h$	54.06 [W/Km^2]	55.7 (+3%)	78.4 (+45%)
$\theta_3 = C_p$	2108 [J/kgK]	2171 (+3%)	3372 (+60%)
$\theta_4 = R_s$	7.8 [$m\Omega$]	8 (+2.56%)	11.7 (+50%)
$\theta_5 = T_{amb}$	25 [°C]	26 (+4%)	29 (+16%)

the maximum pressure threshold P_{max}, whereas the robust controller (with robustness parameter $|\underline{\rho_i}| = 0.9 \times 10^{-5}$) successfully maintains pressure levels within the safety limits. This demonstrates the efficacy of the robust formulation in handling model uncertainty and preventing constraint violations. In both tests, the nominal and robust CBF strategies respect the maximum temperature $T_{\max}$. These results suggest that the nominal controller is more robust in enforcing temperature limits than pressure limits.

A promising direction for future work is the adaptive tuning of the robustness parameter $\underline{\rho_i}$ in real time, based on the level of model uncertainty detected during operation, to better balance safety and performance.

7. Conclusions

In this work, we developed and validated an optimization-based CBF controller designed to safely de-energize a battery cell during emergencies. The controller ensures that critical safety constraints (cell's temperature and pressure), remain within safe limits, mitigating the risk of venting and thermal runaway. To keep the implementation tractable, we employed a simplified equivalent circuit model for the electro-thermal dynamics and approximated the nonlinear pressure equations via a polynomial representation, thereby reducing both computational and design complexity. Furthermore, we derived sufficient conditions to ensure that the CBF-based optimization problem remains numerically feasible. Compared to state-of-the-art MPC, our method is more than 15 times faster, making it suitable for real-time and embedded applications. Another important contribution of this work was the design of a state estimator for SEI decomposition. We proposed an EKF formulation to estimate SEI decomposition using non-invasive data from temperature, voltage, and cell expansion sensors. Validation against a high-fidelity SPMe model further confirmed the effectiveness of the proposed CBF-EKF-based controller, which successfully enforced the safety constraints despite parameter uncertainties of up to 60%.

In future work, we plan to incorporate a disturbance observer within the robust controller framework to reduce conservatism and further enhance safety and performance. The EKF-based state estimator can be further improved by adopting advanced strategies, such as adaptive covariance tuning methods that account for noise cross-correlation through off-diagonal terms in the process noise matrix $\tilde{Q}$. Moreover, full experimental validation of the proposed control and estimation strategy for emergency discharge will be pursued. This study assumed the availability of an emergency discharge hardware capable of handling the energy extracted from the battery. While cell- or module-level discharge can be achieved using off-the-shelf devices such as resistive loads, pack-level presents significant hardware challenges. The design and integration of such high-power discharge devices, particularly for mobile applications, remains an open challenge for practical implementation.

Appendix A. Experimental Validation of the SPMe Under External Short-Circuit Conditions

Figure A.19 compares the SPMe output with the experimental data from a 15-minute External Short Circuit (ESC) test performed with four difference cells described in [39] . The model parameters were fitted only to the first cell (Cell 100A), and applied without retuning to the remaining cases. The observed discrepancies in discharge current between simulation and experiment stem from the constant-resistance discharge mode of the ESC setup, in which the current is algebraically determined by the instantaneous voltage and fixed resistance. Consequently, model mismatches in parameters affecting internal resistance, such as diffusion coefficients or electrolyte conductivity, propagate as voltage errors and, in turn, lead to current deviations. For the short-circuit experiments shown in Figure A.19, the model achieves root-mean-square errors on the order of 0.04-0.05 V for terminal voltage, 1.2-2.3 A/Ah for current, and approximately 9-24°C for maximum temperature, depending on the cell configuration. For non-venting cases, the error in maximum cell expansion stress remains below 3 kPa, while larger discrepancies are observed in venting scenarios due to the highly nonlinear dynamics. All RMSE values were computed over a 15-minute validation window; for venting cells, stress errors were evaluated only up to the onset of venting.

Appendix B. Lipschitz Continuity Analysis

This appendix verifies that the system matrices and nonlinear functions introduced in Table 1 satisfy local Lipschitz continuity with respect to their arguments.

- g_2 is a constant matrix, hence Lipschitz with every $L_2 > 0$.
- $g_1(z)$ is a locally Lipschitz function since [45, Lemma 3.1 Chap. 3]:

  $$\left\|\frac{\partial g_1(z_2)}{\partial z_2}\right\| = \left\|\frac{1}{m_{cell}C_p}\right\| \le L_1. \tag{B.1}$$

  Hence $g_1(z)$ is locally Lipschitz for every $L_1 \ge \frac{1}{m_{cell}C_p}$
- Considering the function $f(x)$, the first component, $f_1(x)$, is a linear function of x_1 and is independent of x_2. The second component, $f_2(x)$, involves an exponential term that depends inversely on x_1. Both partial derivatives of f with respect to x_1 and x_2 exist, and are continuous for all $x_1 > 0$, which guarantees local Lipschitz continuity. The Jacobian matrix of $f(x)$ is given by:

  $$\frac{\partial f}{\partial x} = \begin{bmatrix} -\frac{hA_{\text{surf}}}{m_{cell}C_p} & 0 \\ \frac{A_{\text{SEI}}E_{\text{SEI}}x_{\text{SEI},0}}{k_b x_1^2}\exp\left(\frac{-E_{\text{SEI}}}{k_b x_1}\right) & 0 \end{bmatrix}. \tag{B.2}$$

In this application, the domain of interest is restricted to a compact set:

$$x_1 \in [T_{amb}, T_{max}], \quad x_2 \in [0, x_{\text{SEI},0}]. \tag{B.3}$$

Within this domain, the Jacobian of $f(x)$ remains bounded and thus $f(x)$ is Lipschitz.

Appendix C. Thermal Constraint Feasibility Proof

The proof is composed of the following three parts:

- **Part 1:** consider $\dot{c}_1(z,u) \ge -\alpha_1(c_1(z))$. Recall that $-\alpha_1(c_1(z))$ is negative for $\forall z \in C$. As a result, if $\dot{c}_1(z,u) \ge 0$, $\forall z \in C$, then the original inequality ($\dot{c}_1(z,u) \ge -\alpha_1(c_1(z))$) will be fulfilled for all $z \in C$. We show that $\dot{c}_1(z,u) \ge 0$, or: $-\frac{u}{Q} \ge 0$. The candidate control input $u = 0$ satisfies this inequality.

- **Part 2:** consider $\dot{c}_2(x,z,u) \ge -\alpha_2(c_2(x))$. If $z \in C$, then we need to fulfill $\dot{c}_2(x,z,u) \ge 0$, or:

  $$-\frac{R_s u^2 + V_1 u - hA_{\text{surf}}(T - T_{amb})}{m_{cell}C_p} \ge 0. \tag{C.1}$$

  Since the denominator is always positive, and considering the candidate control input $u = 0$, we have:

  $$hA_{\text{surf}}(T - T_{amb}) \ge 0. \tag{C.2}$$

  This inequality holds since $hA_{\text{surf}} > 0$ and we assumed that $T \ge T_{amb}$.

- **Part 3:** consider $\dot{c}_3(x,z,u) \ge -\alpha_3(c_3(x))$. If $z \in C$, then we need to fulfill $\dot{c}_3(x,z,u) \ge 0$, or:

  $$\left(\frac{R_s u^2 + V_1 u}{m_{cell}C_p} - \frac{hA_{\text{surf}}(T - T_{amb})}{m_{cell}C_p}\right)\frac{\partial \Delta x^{n,max}_{\text{SEI}}(T)}{\partial T}$$
  $$-A_{\text{SEI}}x_{\text{SEI},0}\exp\left(-\frac{E_{\text{SEI}}}{k_b T}\right) \ge 0. \tag{C.3}$$

  Considering $u = 0$, (C.3) can be re-written as:

  $$\begin{aligned} \frac{\partial \Delta x^{n,max}_{\text{SEI}}(T)}{\partial T} &\le -\frac{m_{cell}C_p A_{\text{SEI}}x_{\text{SEI},0}}{hA_{\text{surf}}}\frac{\exp\left(-\frac{E_{\text{SEI}}}{k_b T}\right)}{T - T_{amb}} \\ &\le -k_f\frac{\exp\left(-\frac{E_{\text{SEI}}}{k_b T}\right)}{T - T_{amb}}, \end{aligned}$$

  where $k_f = \frac{m_{cell}C_p A_{\text{SEI}}x_{\text{SEI},0}}{hA_{\text{surf}}}$. This inequality holds due to assumption (ii) stated in Theorem 1.

Combining **Parts 1**, **2**, and **3** demonstrate that $u = 0$ is always a feasible input; hence $\mathcal{U}_{CBF}(z,x) \ne \emptyset$ for every $(z,x) \in C$.

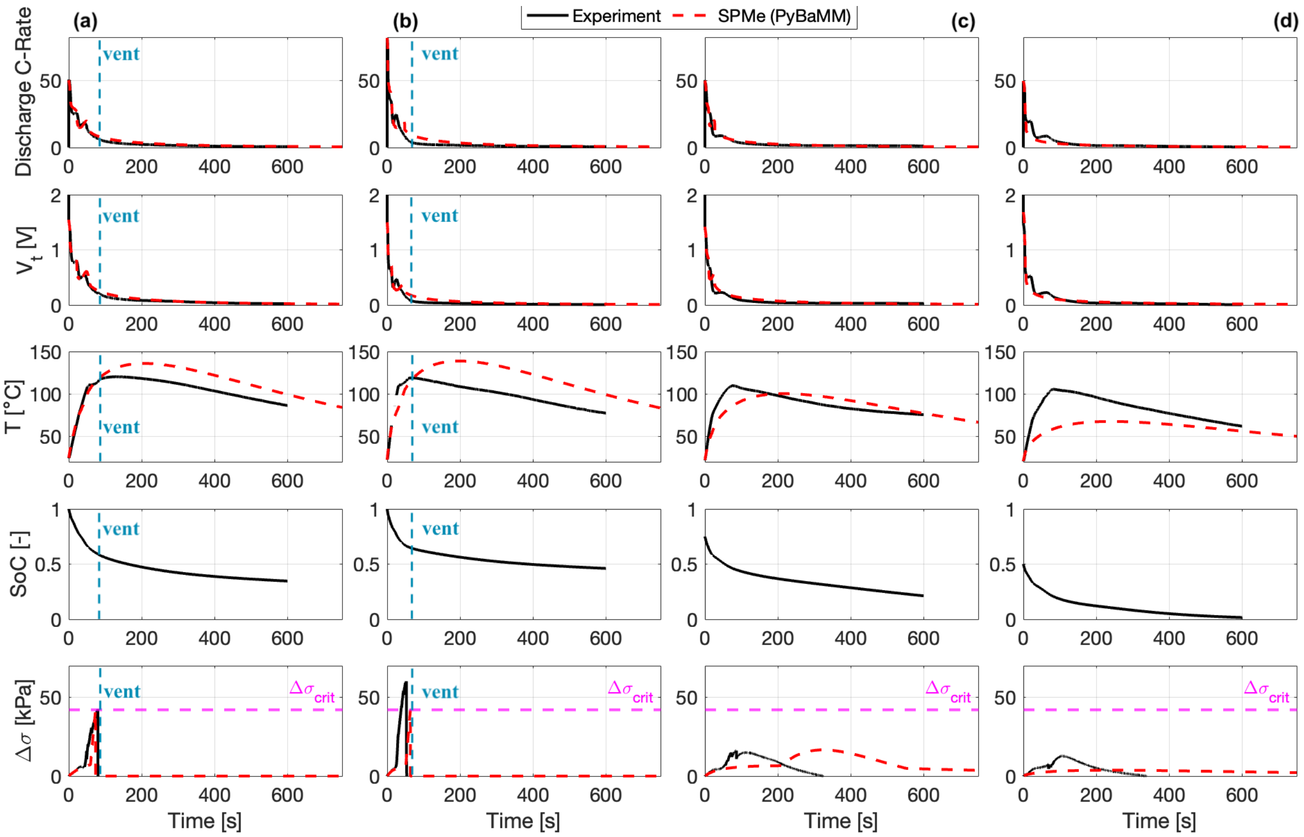

Figure A.19: Comparison between experimental and simulated external short circuit responses at different initial SoC levels ((a) Cell 100A, (b) Cell 100B, (c) Cell 75, (d) Cell 50). The simulations are obtained from the combined multiphysics model (SPMe) using parameters fitted to the Cell 100A (first column (a)) and applied across all cases. The plots show current, voltage, temperature, SoC, and compresive stress evolution over a 15-minute experiment. The experimental data from [39].

Appendix D. Proof of Convexity

According to [56], an optimization program written in the standard form (D.1) is convex if the cost function $f(x)$ and all inequality constraint functions $h_i(x)$ are convex functions.

$$\underset{x}{\text{minimize}} \quad f(x) \tag{D.1a}$$

$$\text{subject to} \quad h_i(x) \le b_i \quad i = 1, \dots, m \tag{D.1b}$$

Furthermore, by the second-order convexity condition, assuming that f is twice differentiable, i.e. its Hessian $\nabla_x^2 f(x)$ exists at each point in the domain of f, then f is convex if and only if the domain f is convex, and its Hessian is positive semi-definite, i.e. $\nabla_x^2 f(x) \ge 0$.

We now apply these results to prove convexity of the optimization problem (29). The cost function $L_{CBF}(u) = (u - I^{\star}_{disch})^2$ on the convex domain $\mathcal{U} \to \mathbb{R}$ is strictly convex since it is quadratic (with positive second-order derivative). Furthermore, the control action $u \in \mathcal{U}$ must fulfill the barrier constraints with linear extended class functions (26) - (28), which can be rewritten in the standard form:

$$h_1(u) = \frac{u}{Q} - K_Q(SoC - SoC_{min}) \le 0, \tag{D.2}$$

$$\begin{aligned} h_2(u) = {} & \frac{R_s u^2 + V_1 u - hA_{\text{surf}}(T - T_{amb})}{m_{cell} C_p} \\ & - K_T(T_{max} - T) \le 0, \end{aligned} \tag{D.3}$$

$$\begin{aligned} h_3(u) = {} & A_{\text{SEI}} x_{\text{SEI},0} \exp\left(-\frac{E_{\text{SEI}}}{k_b T}\right) \\ & - \frac{R_s u^2 + V_1 u - hA_{\text{surf}}(T - T_{amb})}{m_{cell} C_p} \frac{\partial \Delta x^{n,max}_{\text{SEI}}}{\partial T} \\ & - K_P(\Delta x^{n,max}_{\text{SEI}}(T) - \Delta x_{\text{SEI}}) \le 0, \end{aligned} \tag{D.4}$$

where K_Q, K_T, and K_P are the gains of the linear class-$\mathcal{K}$ functions $\alpha_i(\cdot)$, listed in Table 5. To conclude that the problem is convex, we must demonstrate that $h_i(u)$ is convex for all $i = \{1, 2, 3\}$. The function $h_1(u)$ (D.2) is convex since it is an affine function in u (the second derivative of h_1 is zero). To test the convexity of the second constraint (D.3), we compute its second derivative:

$$\frac{\partial^2 h_2(u)}{\partial u^2} = \frac{2R_s}{m_{cell} C_p} > 0, \tag{D.5}$$

which is always positive given that R_s, C_p, m_{cell} are positive constants, hence h_2 is a convex function. Lastly, for $h_3(u)$ we have:

$$\frac{\partial^2 h_3(u)}{\partial u^2} = \frac{-2R_s}{m_{cell}C_p}\frac{\partial \Delta x_{\mathrm{SEI}}^{n,max}(T)}{\partial T}. \tag{D.6}$$

The sign of (D.6) depends on $\frac{\partial \Delta x_{\mathrm{SEI}}^{n,max}(T)}{\partial T}$ which is assumed to be lower than the bound $\Gamma^{max}(T)$ from Theorem 1. As depicted in Figure 9, $\frac{\partial \Delta x_{\mathrm{SEI}}^{n,max}}{\partial T} < 0$ over the operating range, hence $\frac{\partial^2 h_3(u)}{\partial u^2} > 0$. As the cost function is convex and all inequality constraints are convex, the optimization problem is also convex [56], ensuring that any local minimum is the global optimum.

Appendix E. Derivation of the Robustness Parameter from Uncertainty Bounds

The CBF robustness parameter $\underline{\rho_i}$, which enables the design of CBFs that are robust against additive disturbances d, can be computed as:

$$\underline{\rho_i} = \min_{x\in\mathcal{X},\, z\in\mathcal{Z},\, d\in D} \frac{\partial c_i}{\partial x} g_d(x,z)\, d = \min_{x\in\mathcal{X},\, z\in\mathcal{Z},\, d\in D} \rho_i(x,z,d), \tag{E.1}$$

where $\mathcal{X} = \{x = [T, \Delta x_{\mathrm{SEI}}]^\top : \; T_{min} \le x_1 \le T_{max}, \Delta x_{\mathrm{SEI}}^{min} \le x_2 \le \Delta x_{\mathrm{SEI}}^{max}\}$ and $\mathcal{Z}$ represent the expected operating range of the battery and $c_i(\cdot)$ is the CBF constraint.

To better understand how to determine $\underline{\rho_i}$, we focus on parametric uncertainties in the Δx_{SEI} dynamics. Assume that the parameter A_{SEI} is expressed as $A_{\mathrm{SEI}} = A_{\mathrm{SEI}}^\star + d$, where $A_{\mathrm{SEI}}^\star$ is the nominal value and $d \in D = [-\Delta A_{\mathrm{SEI}}^{max}, \Delta A_{\mathrm{SEI}}^{max}]$ the uncertainty range. Inserting this relation into the vector field leads to:

$$f(x) = f^\star(x) + g_d(x)d, \tag{E.2}$$

where $f^\star(x)$ is the nominal vector field and $g_d(x)d$ is the additive disturbance caused by the parametric uncertainty. For an uncertain A_{SEI} , these functions are given by:

$$f^\star(x) = \begin{bmatrix} -\frac{hA_{surf}(x-T_{amb})}{m_{cell}C_p} \\ A_{\mathrm{SEI}}^\star x_{\mathrm{SEI},0}\exp\left(-\frac{E_{\mathrm{SEI}}}{k_b x_1}\right) \end{bmatrix} \tag{E.3a}$$

$$g_d(x) = \begin{bmatrix} 0 \\ x_{\mathrm{SEI},0}\exp\left(-\frac{E_{\mathrm{SEI}}}{k_b x_1}\right) \end{bmatrix}. \tag{E.3b}$$

To ensure robustness to the disturbance $d \in D$, we compute the lower bound:

$$\underline{\rho_i} = \min_{x\in\mathcal{X}, d\in D} \frac{\partial c_i}{\partial x} g_d(x)d, \tag{E.4}$$

which can be expressed as:

$$\underline{\rho_i} = \min_{x\in\mathcal{X}, d\in D} \frac{\partial c_i}{\partial x_2} x_{\mathrm{SEI},0}\exp\left(-\frac{E_{\mathrm{SEI}}}{k_b x_1}\right)d. \tag{E.5}$$

This value is determined by considering the extreme values of each component, leading to:

$$\underline{\rho_i} = -\left|\frac{\partial c_i}{\partial x_2}\right| x_{\mathrm{SEI},0}\exp\left(-\frac{E_{\mathrm{SEI}}}{k_b x_1}\right)\Delta A_{\mathrm{SEI}}^{max}. \tag{E.6}$$

Evaluating $\frac{\partial c_i}{\partial x_2}$ for $i = \{1,2,3\}$, we obtain:

$$\underline{\rho_i} = \begin{cases} 0, & \text{if } \quad i = 1,2 \\ -x_{\mathrm{SEI},0}\exp\left(-\frac{E_{\mathrm{SEI}}}{k_b x_1}\right)\Delta A_{\mathrm{SEI}}^{max}, & \text{if } \quad i = 3 \end{cases} \tag{E.7}$$

Similar type of analysis can be applied to compute $\underline{\rho_i}$ when the model is affected by uncertainties in other parameters (h, C_p, R_s, etc.). The last column of Table 7 lists $\underline{\rho_i}$ when the x_2 dynamics are affected by parameter uncertainties.

References

[1] A. Press, Smoke from fire at California lithium battery plant raises concerns about air quality, 2025.

[2] R. Zalosh, P. Gandhi, A. Barowy, Lithium-ion energy storage battery explosion incidents, Journal of Loss Prevention in the Process Industries 72 (2021).

[3] J. Conzen, S. Lakshmipathy, A. Kapahi, S. Kraft, M. DiDomizio, IPOPT, Journal of Loss Prevention in the Process Industries 81 (2023).

[4] HotCars, An Electric Bus Caught Fire And Set Those Nearby Ablaze, https://www.hotcars.com/an-electric-bus-caught-fire-and-set-those-nearby-ablaze/, 2021.

[5] Q. Wang, P. Ping, X. Zhao, G. Chu, J. Sun, C. Chen, Thermal runaway caused fire and explosion of lithium ion battery, Journal of Power Sources 208 (2012) 210–224. URL: `https://www.sciencedirect.com/science/article/pii/S0378775312003989`. doi:`https://doi.org/10.1016/j.jpowsour.2012.02.038`.

[6] C. Xu, Z. Fan, M. Zhang, P. Wang, H. Wang, C. Jin, Y. Peng, F. Jiang, X. Feng, M. Ouyang, A comparative study of the venting gas of lithium-ion batteries during thermal runaway triggered by various methods, Cell Reports Physical Science 4 (2023) 101705. URL: `https://www.sciencedirect.com/science/article/pii/S2666386423005362`. doi:`https://doi.org/10.1016/j.xcrp.2023.101705`.

[7] G. Amba Prasad Rao, S. Shravan Kumar, A review of integrated battery thermal management systems for lithium-ion batteries of electric vehicles, e-Prime - Advances in Electrical Engineering, Electronics and Energy 8 (2024) 100526. URL: `https://www.sciencedirect.com/science/article/pii/S2772671124001086`.

[8] F. Larsson, B.-E. Mellander, Abuse by external heating, overcharge and short circuiting of commercial lithium-ion battery cells, Journal of The Electrochemical Society 161 (2014) A1611. URL: `https://dx.doi.org/10.1149/2.0311410jes`. doi:`10.1149/2.0311410jes`.

[9] A. W. Golubkov, S. Scheikl, R. Planteu, G. Voitic, H. Wiltsche, C. Stangl, G. Fauler, A. Thaler, V. Hacker, Thermal runaway of commercial 18650 Li-ion batteries with LFP and NCA cathodes–impact of state of charge and overcharge, Rsc Advances 5 (2015) 57171–57186.

[10] T. Joshi, S. Azam, C. Lopez, S. Kinyon, J. Jeevarajan, Safety of Lithium-Ion Cells and Batteries at Different States-of-Charge, Journal of The Electrochemical Society 167 (2020) 140547. URL: `https://dx.doi.org/10.1149/1945-7111/abc8c4`. doi:`10.1149/1945-7111/abc8c4`.

[11] X. Zhu, Z. Sun, Z. Wang, H. Wang, N. Lin, C. Shan, Thermal runaway in commercial lithium-ion cells under overheating condition and the safety assessment method: Effects of SoCs, cathode materials and packaging forms, Journal of Energy Storage 68 (2023) 107768. URL: `https://www.sciencedirect.com/science/article/pii/S2352152X23011659`. doi:`https://doi.org/10.1016/j.est.2023.107768`.

[12] U.S. Department of Transportation, Pipeline and Hazardous Materials Safety Administration (PHMSA), Lithium Battery Guide for Shippers, A Compliance Tool for All Modes of Transportation, 2024.

[13] D. Ouyang, B. Liu, J. Huang, Z. Wang, Degradation and safety performance of lithium-ion cells under high-rate charging/discharging scenarios, Process Safety and Environmental Protection 185 (2024) 76–85. URL: `https://www.sciencedirect.com/science/article/pii/S0957582024002830`. doi:`https://doi.org/10.1016/j.psep.2024.03.064`.

[14] P. Rahmani, S. Chakraborty, I. Mele, T. Katrašnik, S. Bernhard, S. Pruefling, S. Wilkins, O. Hegazy, Driving the future: A comprehensive review of automotive battery management system technologies, and future trends, Journal of Power Sources 629 (2025) 235827. URL: `https://www.sciencedirect.com/science/article/pii/S0378775324017798`. doi:`https://doi.org/10.1016/j.jpowsour.2024.235827`.

[15] V. Tran, J. Siegel, A. Stefanopoulou, Emergency Li-ion Battery Discharge using Nonlinear Model Predictive Control with Temperature and Venting Pressure Constraints, in: 2023 American Control Conference (ACC), 2023, pp. 2500–2505. doi:10.23919/ACC55779.2023.10156473.

[16] I. Ebrahimi, R. de Castro, V. Tran, A. Stefanopoulou, S. Feng, Emergency Battery Discharge under Safety Constraints using Optimization-based Controllers, in: 2024 American Control Conference (ACC), 2024, pp. 3498–3503. doi:10.23919/ACC60939.2024.10644396.

[17] A. D. Ames, X. Xu, J. W. Grizzle, P. Tabuada, Control Barrier Function Based Quadratic Programs for Safety Critical Systems, IEEE Transactions on Automatic Control 62 (2017). doi:10.1109/TAC.2016.2638961.

[18] S. Feng, R. de Castro, I. Ebrahimi, Safe Battery Control Using Cascade-Control-Barrier Functions, IEEE Transactions on Control Systems Technology 32 (2024) 2344–2358. doi:10.1109/TCST.2024.3430708.

[19] M. Kossek, M. S. Trimboli, A Computationally Efficient Control Barrier Function Approach to Safe Lithium-ion Battery Charging, in: 2025 American Control Conference, 2025, pp. 2799–2804.

[20] M. Charkhgard, M. Farrokhi, State-of-Charge Estimation for Lithium-Ion Batteries Using Neural Networks and EKF, IEEE Transactions on Industrial Electronics 57 (2010) 4178–4187. doi:10.1109/TIE.2010.2043035.

[21] Z. Wang, D. T. Gladwin, M. J. Smith, S. Haass, Practical state estimation using Kalman filter methods for large-scale battery systems, Applied Energy 294 (2021) 117022. URL: https://www.sciencedirect.com/science/article/pii/S0306261921004852. doi:https://doi.org/10.1016/j.apenergy.2021.117022.

[22] Y. Kim, S. Mohan, J. B. Siegel, A. G. Stefanopoulou, Y. Ding, The Estimation of Temperature Distribution in Cylindrical Battery Cells Under Unknown Cooling Conditions, IEEE Transactions on Control Systems Technology 22 (2014) 2277–2286. doi:10.1109/TCST.2014.2309492.

[23] K. Mc Carthy, H. Gullapalli, T. Kennedy, Real-time internal temperature estimation of commercial Li-ion batteries using online impedance measurements, Journal of Power Sources 519 (2022) 230786. URL: https://www.sciencedirect.com/science/article/pii/S0378775321012775. doi:https://doi.org/10.1016/j.jpowsour.2021.230786.

[24] M. B. Pinson, M. Z. Bazant, Theory of SEI Formation in Rechargeable Batteries: Capacity Fade, Accelerated Aging and Lifetime Prediction, Journal of The Electrochemical Society 160 (2012) A243. URL: https://doi.org/10.1149/2.044302jes. doi:10.1149/2.044302jes.

[25] C. Zu, H. Yu, H. Li, Enabling the thermal stability of solid electrolyte interphase in li-ion battery, InfoMat 3 (2021) 648–661. doi:https://doi.org/10.1002/inf2.12190.

[26] C. He, Q. Yue, Q. Chen, T. Zhao, Modeling thermal runaway of lithium-ion batteries with a venting process, Applied Energy 327 (2022) 120110. URL: https://www.sciencedirect.com/science/article/pii/S0306261922013678. doi:https://doi.org/10.1016/j.apenergy.2022.120110.

[27] S. Wang, Q. Wang, L. Xu, Y. Sun, X. Feng, H. Wang, A review on mechanisms, characteristics and relating hazards of vent gases from thermally abused Li-ion batteries, Journal of Energy Storage 84 (2024) 110892. URL: https://www.sciencedirect.com/science/article/pii/S2352152X24004766. doi:https://doi.org/10.1016/j.est.2024.110892.

[28] J. Wu, M. Ihsan-Ul-Haq, Y. Chen, J.-K. Kim, Understanding solid electrolyte interphases: Advanced characterization techniques and theoretical simulations, Nano Energy 89 (2021) 106489. URL: https://www.sciencedirect.com/science/article/pii/S2211285521007424. doi:https://doi.org/10.1016/j.nanoen.2021.106489.

[29] J. Lin, W. Hu, J. Yang, L. Pan, X. Xia, Y. Wei, Z. Gong, Y. Yang, Revisiting High-Frequency Impedance in Li-Ion Batteries: Decoupling Solid Electrolyte Interphase Resistance from Pore Impedance, The Journal of Physical Chemistry Letters 16 (2025) 7490–7497.

[30] M. Steinhauer, S. Risse, N. Wagner, K. A. Friedrich, Investigation of the Solid Electrolyte Interphase Formation at Graphite Anodes in Lithium-Ion Batteries with Electrochemical Impedance Spectroscopy, Electrochimica Acta 228 (2017) 652–658. URL: https://www.sciencedirect.com/science/article/pii/S0013468617301639. doi:https://doi.org/10.1016/j.electacta.2017.01.128.

[31] F. Santoni, A. De Angelis, A. Moschitta, P. Carbone, M. Galeotti, L. Cinà, C. Giammanco, A. Di Carlo, A guide to equivalent circuit fitting for impedance analysis and battery state estimation, Journal of Energy Storage 82 (2024) 110389. URL: https://www.sciencedirect.com/science/article/pii/S2352152X2303788X. doi:https://doi.org/10.1016/j.est.2023.110389.

[32] G. L. Plett, Extended Kalman filtering for battery management systems of LiPB-based HEV battery packs: Part 1. Background, Journal of Power Sources 134 (2004) 252–261. URL: https://www.sciencedirect.com/science/article/pii/S0378775304003593. doi:https://doi.org/10.1016/j.jpowsour.2004.02.031.

[33] Y. Huang, T. Wang, W. Xu, Y. Zhao, Y. Liao, J. Wang, Y. Fan, Z. Wang, Study on thermal runaway characteristics of lithium batteries under high-rate charge/discharge and development of a deep learning-based early warning model, Energy 334 (2025) 137676. URL: https://www.sciencedirect.com/science/article/pii/S0360544225033183. doi:https://doi.org/10.1016/j.energy.2025.137676.

[34] L. A. Vu, H. S. Hong, L. T. Quang, P. Van Giang, D. T. Binh, N. D. Thuan, N. H. Ha, A real-time framework for early detection and severity prediction of thermal runaway in Li-ion batteries, Journal of Energy Storage 135 (2025) 118310. URL: https://www.sciencedirect.com/science/article/pii/S2352152X25030233. doi:https://doi.org/10.1016/j.est.2025.118310.

[35] National Highway Traffic Safety Administration, Federal Motor Vehicle Safety Standards; Electric Powertrain Integrity; Documentation for Thermal Propagation Safety Due to Single-Cell Thermal Runaway and Internal Short Circuit, Proposed Rule, 89 FR 104318 (Dec. 20, 2024), 2024. URL: https://www.govinfo.gov/content/pkg/FR-2024-12-20/html/2024-28707.htm.

[36] K.-Y. Lo, Y.-M. Chen, Y.-R. Chang, Bidirectional Single-Stage Grid-Connected Inverter for a Battery Energy Storage System, IEEE Transactions on Industrial Electronics 64 (2017) 4581–4590. doi:10.1109/TIE.2016.2559453.

[37] V. Tran, T. Cai, A. Stefanopoulou, J. B. Siegel, Equivalent Circuit Model for High C-Rate Discharge with an External Short Circuit, in: American Control Conference, 2022, pp. 1782–1787. doi:10.23919/ACC53348.2022.9867199.

[38] P. T. Coman, E. C. Darcy, C. T. Veje, R. E. White, Modelling Li-Ion Cell Thermal Runaway Triggered by an Internal Short Circuit Device Using an Efficiency Factor and Arrhenius Formulations, Journal of The Electrochemical Society 164 (2017). doi:10.1149/2.0341704jes.

[39] V. Tran, J. B. Siegel, A. G. Stefanopoulou, Extending a Multiphysics Li-Ion Battery Model from Normal Operation to Short Circuit and Venting, Journal of The Electrochemical Society 171 (2024). URL: https://dx.doi.org/10.1149/1945-7111/ad5110. doi:10.1149/1945-7111/ad5110.

[40] T. Cai, V. Tran, A. G. Stefanopoulou, J. B. Siegel, Modeling Li-ion Battery First Venting Events Before Thermal Runaway, IFAC-PapersOnLine 54 (2021). Modeling, Estimation and Control Conference.

[41] S. G. Marquis, V. Sulzer, R. Timms, C. P. Please, S. J. Chapman, An asymptotic derivation of a single particle model with electrolyte, Journal of The Electrochemical Society 166 (2019). URL: https://dx.doi.org/10.1149/2.0341915jes. doi:10.1149/2.0341915jes.

[42] T. D. Hatchard, D. D. MacNeil, A. Basu, J. R. Dahn, Thermal Model of Cylindrical and Prismatic Lithium-Ion Cells, Journal of The Electrochemical Society 148 (2001). URL: https://dx.doi.org/10.1149/1.1377592. doi:10.1149/1.1377592.

[43] C. Fear, D. Juarez-Robles, J. A. Jeevarajan, P. P. Mukherjee, Elucidating Copper Dissolution Phenomenon in Li-Ion Cells under Overdischarge Extremes, Journal of The Electrochemical Society 165 (2018) A1639. URL: https://dx.doi.org/10.1149/2.0671809jes. doi:10.1149/2.0671809jes.

[44] R. Guo, L. Lu, M. Ouyang, X. Feng, Mechanism of the entire overdischarge process and overdischarge-induced internal short circuit in lithium-ion batteries, Scientific reports 6 (2016) 30248.

[45] H. Khalil, Nonlinear Systems, Pearson Education, Prentice Hall, 2002.

[46] A. Allam, S. Onori, Linearized Versus Nonlinear Observability Analysis for Lithium-Ion Battery Dynamics: Why Respecting the Nonlinearities Is Key for Proper Observer Design, IEEE Access 9 (2021). doi:10.1109/

ACCESS.2021.3130631.

[47] R. Hermann, A. Krener, Nonlinear controllability and observability, IEEE Transactions on Automatic Control 22 (1977) 728–740. doi:10.1109/TAC.1977.1101601.

[48] J. Pukrushpan, A. Stefanopoulou, S. Varigonda, J. Eborn, C. Haugstetter, Control-oriented model of fuel processor for hydrogen generation in fuel cell applications, Control Engineering Practice 14 (2006) 277–293. URL: https://www.sciencedirect.com/science/article/pii/S0967066105001371. doi:https://doi.org/10.1016/j.conengprac.2005.04.014, advances in Automotive Control (AC'04).

[49] J. N. E. Lucero, S. Onori, Comparative Nonlinear Observability Analysis of Spatial Discretization Schemes for Lithium-Ion Battery Models, in: 2025 American Control Conference (ACC), 2025, pp. 2805–2810. doi:10.23919/ACC63710.2025.11107574.

[50] MathWorks, Extended kalman filters, 2024. https://www.mathworks.com/help/fusion/ug/extended-kalman-filters.html.

[51] H. Khalil, Nonlinear Control, Always Learning, Pearson, 2014.

[52] C. Liu, X. Xiang, Y. Duan, L. Yang, S. Yang, Improved path following for autonomous marine vehicles with low-cost heading/course sensors: comparative experiments, Control Engineering Practice 142 (2024) 105740. URL: https://www.sciencedirect.com/science/article/pii/S096706612300309X. doi:https://doi.org/10.1016/j.conengprac.2023.105740.

[53] J. Löfberg, YALMIP : A Toolbox for Modeling and Optimization in MATLAB, in: In Proceedings of the CACSD Conference, 2004, pp. 284–289.

[54] A. Wächter, L. Biegler, On the implementation of an interior-point filter line-search algorithm for large-scale nonlinear programming, Mathematical Programming 106 (2006).

[55] S. D. Vyas, T. Roy, S. Dey, An Input-to-State Safety Approach Toward Thermal Fault-Tolerant Battery Cells, IEEE Transactions on Control Systems Technology 32 (2024) 1647–1658. doi:10.1109/TCST.2023.3345130.

[56] S. Boyd, L. Vandenberghe, Convex Optimization, Cambridge University Press, 2004.